

This is a repository copy of *Oxidative desulfurization pathway for complete catabolism of sulfoquinovose by bacteria*.

White Rose Research Online URL for this paper:

<https://eprints.whiterose.ac.uk/id/eprint/182057/>

Version: Accepted Version

---

**Article:**

Sharma, Mahima [orcid.org/0000-0003-3960-2212](https://orcid.org/0000-0003-3960-2212), Lingford, James P, Petricevic, Marija et al. (15 more authors) (2022) Oxidative desulfurization pathway for complete catabolism of sulfoquinovose by bacteria. *Proceedings of the National Academy of Sciences of the United States of America*. e2116022119. ISSN: 1091-6490

<https://doi.org/10.1073/pnas.2116022119>

---

**Reuse**

Items deposited in White Rose Research Online are protected by copyright, with all rights reserved unless indicated otherwise. They may be downloaded and/or printed for private study, or other acts as permitted by national copyright laws. The publisher or other rights holders may allow further reproduction and re-use of the full text version. This is indicated by the licence information on the White Rose Research Online record for the item.

**Takedown**

If you consider content in White Rose Research Online to be in breach of UK law, please notify us by emailing [eprints@whiterose.ac.uk](mailto:eprints@whiterose.ac.uk) including the URL of the record and the reason for the withdrawal request.

**Main Manuscript for**

**Oxidative desulfurization pathway for complete catabolism of sulfoquinovose by bacteria**

Mahima Sharma,<sup>1</sup> James P. Lingford,<sup>2,3</sup> Marija Petricevic,<sup>4,5</sup> Alexander J.D. Snow,<sup>1</sup> Yunyang Zhang,<sup>4,5</sup> Michael A. Järvå,<sup>2,3</sup> Janice W.-Y. Mui,<sup>4,5</sup> Nichollas E. Scott,<sup>6</sup> Eleanor C. Saunders,<sup>7</sup> Runyu Mao,<sup>2,3</sup> Ruwan Epa,<sup>4,5</sup> Bruna M. da Silva,<sup>7,8</sup> Douglas E.V. Pires,<sup>7,8</sup> David B. Ascher,<sup>5,7</sup> Malcolm J. McConville,<sup>7</sup> Gideon J. Davies,<sup>1\*</sup> Spencer J. Williams,<sup>4,5\*</sup> Ethan D. Goddard-Borger<sup>2,3\*</sup>

<sup>1</sup> York Structural Biology Laboratory, Department of Chemistry, University of York, Heslington, YO10 5DD, U.K.

<sup>2</sup> The Walter and Eliza Hall Institute of Medical Research, Parkville, Victoria 3052, Australia.

<sup>3</sup> Department of Medical Biology, University of Melbourne, Parkville, Victoria 3010, Australia.

<sup>4</sup> School of Chemistry, University of Melbourne, Parkville, Victoria 3010, Australia.

<sup>5</sup> Bio21 Molecular Science and Biotechnology Institute, University of Melbourne, Parkville, Victoria 3010, Australia

<sup>6</sup> Department of Microbiology and Immunology, University of Melbourne at the Peter Doherty Institute for Infection and Immunity, Parkville, Victoria 3010, Australia.

<sup>7</sup> Department of Biochemistry and Pharmacology, Bio21 Molecular Science and Biotechnology Institute, University of Melbourne, Parkville, Victoria 3010, Australia

<sup>8</sup> School of Computing and Information Systems, University of Melbourne, Melbourne, Victoria 3010, Australia

**Gideon J. Davies**

**Email:** gideon.davies@york.ac.uk

**Spencer J. Williams**

30 **Email:** sjwill@unimelb.edu.au

31 **Ethan D. Goddard-Borger**

32 **Email:** goddard-borger.e@wehi.edu.au

33

34 **Author Contributions**

35 EDG-B discovered the SMO gene cluster; SJW, EDG-B, GJD conceived project; MP and JW-YM  
36 conducted microbial growth experiments; NES conducted proteomics; JPL, MS, AS, MJ performed  
37 molecular biology, protein expression and structural and biophysical characterization; YZ, JPL, AS,  
38 MS, RM performed biochemical assays; ECS and MJM conducted carbohydrate analysis; YZ, JW-  
39 YM, BM and DA performed bioinformatics analysis; SJW, MS, EGB wrote the paper with input  
40 from all authors.

41

42 **Competing Financial Interests Statement**

43 The authors declare no competing interests.

44

45 **Classification:** Physical Science/Chemistry  
46 Biological Science/Biochemistry

47

48 **Keywords:** carbohydrate metabolism, sulfur cycle, oxidative desulfurization

49

50 **This PDF file includes:**

51 Main Text

52 Figures 1 to 5

53 *Abstract*

54 Catabolism of sulfoquinovose (SQ, 6-deoxy-6-sulfoglucose), the ubiquitous sulfosugar produced by  
55 photosynthetic organisms, is an important component of the biogeochemical carbon and sulfur  
56 cycles. Here, we describe a new pathway for SQ degradation that involves oxidative desulfurization  
57 to release sulfite and enable utilization of the entire carbon skeleton of the sugar to support the  
58 growth of the plant pathogen *Agrobacterium tumefaciens*. SQ or its glycoside sulfoquinovosyl  
59 glycerol (SQGro) are imported into the cell by an ABC transporter system with an associated SQ  
60 binding protein. A sulfoquinovosidase hydrolyses the SQ glycoside and the liberated SQ is acted on  
61 by a flavin mononucleotide-dependent sulfoquinovose monooxygenase, in concert with an NADH-  
62 dependent flavin reductase, to release sulfite and 6-oxo-glucose. An NADPH-dependent  
63 oxidoreductase reduces the 6-oxo-glucose to glucose, enabling entry into primary metabolic  
64 pathways. Structural and biochemical studies provide detailed insights into the recognition of key  
65 metabolites by proteins in this pathway. Bioinformatic analyses reveal that the sulfoquinovose  
66 monooxygenase (smo) pathway is distributed across Alpha- and Betaproteobacteria and is  
67 especially prevalent within the Rhizobiales order. This strategy for SQ catabolism is distinct from  
68 previously described pathways as it enables the complete utilization of all carbons within SQ by a  
69 single organism with concomitant production of inorganic sulfite.

70

71

72 *Significance Statement*

73 Sulfoquinovose, a sulfosugar derivative of glucose, is produced by most photosynthetic organisms  
74 and contains up to half of all sulfur in the biosphere. Several pathways for its breakdown are  
75 known, though they provide access to only half of the carbon in sulfoquinovose and none of its  
76 sulfur. Here, we describe a fundamentally different pathway within the plant pathogen  
77 *Agrobacterium tumefaciens* that features oxidative desulfurization of sulfoquinovose to access all  
78 carbon and sulfur within the molecule. Biochemical and structural analyses of the pathway's key  
79 proteins provided insights how the sulfosugar is recognized and degraded. Genes encoding this  
80 sulfoquinovose monooxygenase pathway are present in many plant pathogens and symbionts,  
81 alluding to a possible role for sulfoquinovose in plant host–bacteria interactions.

82

## 83 **Introduction**

84 Sulfoquinovose (SQ; 6-deoxy-6-sulfoglucose) is an anionic sulfosugar found in plant and  
85 cyanobacterial sulfolipids, and in S-layer proteins in archaea (1). It is estimated that SQ holds  
86 around half of all sulfur in the biosphere, with 10 billion tonnes produced each year in Nature, and  
87 so its cycling is a significant component of the biogeochemical sulfur cycle (2). SQ is primarily  
88 found as the headgroup of the plant sulfolipid sulfoquinovosyl diacylglycerol, and its close  
89 association with photosynthetic membranes and proteins supports roles in their structure and  
90 function (3). Microbial communities play a dominant role in SQ cycling and usually more than one  
91 organism is required to completely assimilate this source of carbon and sulfur. Organisms with a  
92 tier 1 pathway, termed sulfoglycolysis, perform scission of the C3-C4 bond of SQ to give two three-  
93 carbon fragments; carbons 1-3 enter central metabolism, while carbons 4-6 bearing the sulfonate are  
94 excreted as dihydroxypropanesulfonate (DHPS) or sulfolactate (SL). Organisms with a tier 2  
95 pathway are those that process DHPS and SL to access the remaining three carbon fragment and  
96 release inorganic sulfur. To date, three tier 1 pathways have been described: the sulfoglycolytic  
97 Embden-Meyerhof-Parnas (sulfo-EMP) (4), Entner-Doudoroff (sulfo-ED) (5, 6) and sulfofructose  
98 transaldolase (sulfo-SFT) pathways (7, 8). Tier 2 metabolism has been described for various  
99 specialized bacteria that utilize SL or DHPS and perform ‘biomineralization’ to release inorganic  
100 sulfite, which under aerobic conditions is readily oxidized to sulfate (1). While many of the steps in  
101 the three tier 1 sulfoglycolysis pathways differ, all three pathways share the presence of a  
102 specialized glycoside hydrolase, a sulfoquinovosidase (SQase), which catalyzes the hydrolysis of  
103 SQ glycosides, such as SQGro, to release SQ (9, 10).

104  
105 While the tier 1 and 2 pathways described to date require two or more organisms to complete the  
106 ‘biomineralization’ of SQ, there is some evidence that this can also be accomplished by a single  
107 organism. Roy and co-workers have reported that an *Agrobacterium* strain from soil can completely  
108 consume SQ, with release of sulfate, although the genetic and biochemical details behind this  
109 process were not investigated (11). We previously reported that *A. tumefaciens* C58 contains a  
110 functional SQase, with the ability to hydrolyze SQGro (9). However, analysis of its genome did not  
111 reveal any genes homologous to those expected for known tier 1 sulfoglycolysis pathways.

112  
113 Here, we investigate the ‘biomineralization’ of SQ by *Agrobacterium tumefaciens* (*Agrobacterium*  
114 *fabrum*) strain C58 and show that this organism effects the oxidoreductive desulfurization of SQ to  
115 release inorganic sulfite and glucose, which can feed into primary metabolism. We show that this  
116 pathway involves: a novel SQ/SQGro solute binding protein and associated ATP-binding cassette  
117 (ABC) transporter; an SQase to release SQ from its glycosides; a flavin-dependent SQ

118 monooxygenase with paired flavin-reductase to effect oxidative desulfurization of SQ to sulfite and  
119 6-oxo-glucose; and a NADPH-dependent oxidoreductase to reduce 6-oxo-glucose to glucose. X-ray  
120 structures determined for each of these proteins in complex with relevant metabolites reveal the  
121 molecular basis of substrate binding and catalysis. We show through bioinformatics analyses that  
122 this pathway – the first to enable the complete assimilation of SQ – is distributed across Alpha- and  
123 Betaproteobacteria and is particularly well-represented within the Rhizobiales order.  
124

## Results

### *Differential expression of a gene cluster in the presence sulfoquinovose*

To determine if *A. tumefaciens* C58 can utilize SQ as a carbon source, we attempted to grow this organism in M9 minimal media containing SQ as the sole carbon source. *A. tumefaciens* C58 exhibited robust growth in this media and analysis of spent culture supernatant failed to detect DHPS or SL. Instead, the culture supernatant accumulated sulfate, but with a lag between consumption of SQ and sulfate release (**Fig. 1a, Fig. S1**), as was previously reported by Roy and co-workers for *Agrobacterium* sp. strain ABR2 (11). Noting that sulfite is generally released from organosulfonate degradation pathways (1, 12), we analyzed the supernatant for sulfite ( $\text{SO}_3^{2-}$ ), and observed that SQ consumption is coincident with production of sulfite, which slowly undergoes autooxidation to sulfate. To investigate the metabolism of the carbon skeleton of SQ, we cultured *A. tumefaciens* on  $^{13}\text{C}_6$ -SQ (13) and analyzed the culture supernatant using  $^{13}\text{C}$  NMR spectroscopy (**Fig. S2**). The only significant  $^{13}\text{C}$ -labelled product we could detect was  $^{13}\text{C}$ -bicarbonate, which formed transiently during exponential phase growth, and the  $^{13}\text{C}$ -labelled bicarbonate signal disappeared at stationary phase, presumably through exchange with atmospheric  $\text{CO}_2$ . *A. tumefaciens* grew on other sulfoquinovosides, including SQGro and methyl  $\alpha$ -sulfoquinovoside (MeSQ), but did not grow on other alkylsulfonates including DHPS, SL, sulfoacetic acid, taurine, pentanesulfonate, MES, MOPS, HEPES, PIPES, cysteic acid or methanesulfonic acid (**Fig. S3**). Collectively, this data demonstrates that *A. tumefaciens* effects the complete metabolism of the carbon backbone of SQ with concomitant release of sulfite.

We performed comparative proteomic experiments to identify changes associated with the growth of *A. tumefaciens* on SQ compared to glucose at mid-log phase (**Fig. 1b**). The largest and most significant change we observed was an increase in the abundance of proteins encoded by a single cluster of genes (*Atu3277-Atu3285*) for cells grown on SQ. Proteins encoded by *Atu3283* and *Atu3284* were not observed; however, they are predicted to be integral membrane proteins that can be difficult to detect using conventional proteomic workflows (14). Thus, the gene cluster *Atu3277-Atu3285*, which was subsequently renamed *smoA-smoI*, appeared to be important for growth on SQ (**Fig. 1c**). While the protein encoded by *Atu3285* was previously identified as an SQase (9), the proteins encoded by other genes in the cluster were not annotated with functions that were consistent with any tier 1 pathway, suggesting that *A. tumefaciens* uses a different approach for the catabolism of SQ. The automated annotations ascribed to the respective gene products in the cluster, which included a putative ABC transporter system, sulfonate monooxygenase, SDR oxidoreductase, flavin reductase and exporters, enabled development of a hypothetical biochemical pathway that could explain the complete assimilation of SQ by *A. tumefaciens* (**Fig. 1d**). We

160 proceeded to biochemically validate this hypothesis and gain structural insights into the proteins  
161 involved.

162

### 163 *Atu3282 (smoF) encodes an ABC transporter solute-binding protein that binds SQGro*

164 Within the gene cluster identified through proteomics, *Atu3281 (smoE)*, *Atu3283 (smoG)*, and  
165 *Atu3284 (smoH)* were annotated as an ABC transporter system, with *Atu3282 (smoF)* encoding an  
166 associated periplasmic solute-binding protein. The substrate preferences of solute binding proteins  
167 are useful for assigning functions to their associated ABC transporters (15). Accordingly, we  
168 produced recombinant SmoF (**Fig. S4**) and demonstrated that it binds SQGro with  $K_d = 0.29 \pm 0.17$   
169  $\mu\text{M}$  ( $\Delta H = -11 \pm 0.4 \text{ kcal mol}^{-1}$ ,  $\Delta S = -7 \pm 2 \text{ cal mol}^{-1} \text{ deg}^{-1}$ ) (**Fig. 2a, Fig. S5, Table S3**). No binding  
170 was observed for the stereochemically-related monosaccharides D-glucose and D-glucuronic acid.

171

172 To delineate how SmoF recognizes its ligand, we used X-ray diffraction methods to obtain a high-  
173 resolution 3D structure of SmoF in its ligand-free apo state and in complex with SQGro (**Fig. 2b,**  
174 **Table S4**). Like most ABC transporter solute-binding proteins, SmoF possesses two globular  
175 domains with a similar  $\alpha/\beta$  fold forming a deep cleft lined with aromatic and polar residues to  
176 capture the ligand. Comparisons of the structures for ligand-free SmoF and the SQGro complex  
177 revealed a large conformational change in the protein resulting from inter-domain rotation upon  
178 SQGro binding. The relative movement of domains was assessed using the DynDom server, which  
179 indicated a hinge rotation of  $31^\circ$  about four linker regions connecting the two domains (**Fig. S6**).  
180 SQGro is buried deep within the inter-domain cleft and residues from both domains accommodate  
181 this ligand through a network of hydrogen-bonding interactions (**Fig. 2c,d**). The sulfonate of  
182 SQGro, which is the defining feature of this sulfosugar, is accommodated by hydrogen-bonds to the  
183 side-chain of Thr220 (2.6 Å), backbone amides of Gly166 (3 Å) and Ser43 (2.8 Å), and an ordered  
184 water molecule that in turn hydrogen-bonds to the sidechain of His13 (3 Å) and Gln46 (3.2 Å) (**Fig.**  
185 **2c,d**). These and the other interactions in the SQGro-bound ‘closed’ state stabilized SmoF  
186 substantially, as evidenced by a 15 °C increase in the protein melting temperature (**Fig. S7**).

187

### 188 *The structural basis of SQGro recognition by the SQase Atu3285 (SmoI)*

189 We previously reported that *Atu3285 (smoI)* encodes an SQase that preferentially hydrolyses 2'R-  
190 SQGro, the natural stereoisomer of this glycoside (9). To understand the molecular basis of the  
191 preference SmoI has for this stereoisomer, we determined the 3D structure of a pseudo-Michaelis  
192 complex: the inactive acid/base mutant SmoI-D455N in complex with 2'R-SQGro (**Fig. 2e,f**). SmoI-  
193 D455N•SQGro crystallized with four protomers in the asymmetric unit, each showing unambiguous  
194 density of the substrate bound at the active site. As described previously, the overall fold is an



195 ( $\alpha/\beta$ )<sub>8</sub> barrel appended with small  $\beta$  sheet domain and the sulfonate group is recognized by  
196 Arg283/Trp286/Tyr491 triad<sup>8</sup>. Arg438 and Glu135 make hydrogen-bonding interactions with the  
197 glyceryl aglycone of 2'R-SQGro. Only Arg438 interacts with the C2-hydroxyl group of the glyceryl  
198 aglycone and thus this residue appears to drive selectivity for the 2'R-SQGro stereoisomer.  
199

#### 200 *Atu3277 (smoA) encodes a flavin mononucleotide (FMN) reductase*

201 SmoA, annotated as a flavin reductase, was recombinantly expressed in *E. coli* and maintained a  
202 yellow color throughout purification, suggesting that it had co-purified with a flavin co-factor. A  
203 sample of this protein was heat-denatured to release the co-factor and the supernatant analyzed by  
204 LC-MS to reveal that FMN was the sole detectable flavin (**Fig. S8**). Michaelis-Menten kinetics  
205 were conducted for SmoA with saturating FMN and NADH or NADPH to determine which of these  
206 reductants was preferred by the enzyme. With NADH the kinetic parameters were  $K_M = 35 \pm 5 \mu\text{M}$ ,  
207  $k_{\text{cat}} = 14.5 \pm 0.5 \text{ s}^{-1}$  and  $k_{\text{cat}}/K_M = 4.1 \times 10^5 \text{ M}^{-1} \text{ s}^{-1}$ ; while for NADPH saturation was not observed and  
208  $k_{\text{cat}}/K_M = 6.8 \times 10^2 \text{ M}^{-1} \text{ s}^{-1}$ , indicating that NADH is the preferred cofactor for SmoA (**Fig. 3a, Fig.**  
209 **S9, Fig. S10**). Owing to difficulties in obtaining structural data for this enzyme, we also studied a  
210 close homologue from *Rhizobium oryzae* (RoSmoA, UniProt accession number: A0A1X7D6Q3),  
211 which possesses a syntenic gene cluster to *Atu3277-Atu3285*. Recombinant RoSmoA also co-  
212 purified with FMN (**Fig. S8**) and utilized the NADH cofactor with  $K_M = 16 \pm 5 \mu\text{M}$ ,  $k_{\text{cat}} = 33 \pm 2 \text{ s}^{-1}$   
213 and  $k_{\text{cat}}/K_M = 2.1 \times 10^6 \text{ M}^{-1} \text{ s}^{-1}$  (**Fig. S9**).  
214

#### 215 *Atu3279 (smoC) encodes an SQ monooxygenase that desulfurizes SQ*

216 SmoC is annotated as an alkanesulfonate monooxygenase, though it possesses only 30% sequence  
217 identity with the well-characterized alkanesulfonate monooxygenase SsuD, from *E. coli*. SsuD  
218 catalyzes the FMNH<sub>2</sub>- and O<sub>2</sub>-dependent oxidation of alkanesulfonates to produce the  
219 corresponding aldehyde and sulfite, with a preference for pentanesulfonate (16). The mechanism of  
220 this and related enzymes have been intensively studied yet remain enigmatic. The transformation is  
221 thought to involve initial formation of a C4a-peroxy or N5-peroxy flavin species on-enzyme. One  
222 mechanism posits that the terminal peroxide oxygen attacks the sulfonate sulfur of the substrate  
223 before undergoing a rearrangement to effect C-S bond fissure and release of the aldehyde and  
224 sulfite products (**Fig. S12a**) (17). An alternative mechanism suggests the peroxide deprotonates C6,  
225 which is then oxidized to an  $\alpha$ -hydroxysulfonate that undergoes elimination to produce sulfite and  
226 the aldehyde (**Fig. 12b**) (18). To demonstrate activity for recombinant SmoC (**Fig. S4**), we adapted  
227 assays developed for SsuD that use Ellman's reagent to detect sulfite released by the enzyme (19).  
228 Direct detection of the putative sugar product, 6-oxo-glucose (6-OG), is not trivial as this molecule  
229 exists as a complex equilibrium of (hemi)acetals and hydrates that have poor stability. Thus, SmoC

230 was incubated with SQ in the presence of SmoA, FMN and NADH, which generate FMNH<sub>2</sub> *in situ*,  
 231 and the concentration of sulfite determined periodically using Ellman's reagent (**Fig. 3b**). Maximal  
 232 substrate conversion was approximately 200 μM (**Fig. S12c**), which is commensurate with the  
 233 solubility of molecular oxygen in water under standard conditions, with peak activity observed at  
 234 pH 8.5 (**Fig. S12d**). No activity was observed when SQ was replaced with other sulfonates,  
 235 including SQGro (the precursor to SQ) or HEPES (an unrelated sulfonate) demonstrating that,  
 236 unlike the promiscuous SsuD, SmoC has high specificity for SQ (**Fig. S12c**). As such, the  
 237 hydrolysis of SQGro by SmoI necessarily precedes oxidative desulfurization by SmoC. This  
 238 observation is further supported by ITC, where SQ was found to bind SmoC with  $K_d = 3 \mu\text{M}$  in the  
 239 absence of any flavin-based cofactors, whereas no binding was detected for SQGro (**Fig. 3c**, **Fig.**  
 240 **S13**, **Table S3**). The unique SQ monooxygenase activity of SmoC defines this pathway: it is the  
 241 enzyme that effects fissure of the C–S bond in SQ, and so it was chosen as the namesake for this  
 242 gene cluster and *Atu3277-Atu3285* were renamed the **SQ MonoOxygenase** cluster (*smoA-I*).  
 243

244 While we could readily crystallize SmoC, these crystals only diffracted to a maximum resolution of  
 245 3.4 Å. The corresponding low-resolution map suggested that SmoC exists as a dimer, which was  
 246 confirmed in solution by SEC-MALS (**Fig. S14**). To obtain structural information for an SQ  
 247 monooxygenase, we turned to the homolog from *R. oryzae* (*RoSmoC*). Recombinant *RoSmoC*  
 248 exhibited similar activity and substrate selectivity for SQ to SmoC (**Fig. S12e**) and provided  
 249 crystals that diffracted to 1.9 Å. Importantly, the low-resolution structure of *A. tumefaciens* SmoC  
 250 superimposed with the high-resolution *RoSmoC* structures with a peptide backbone rmsd of 0.4 Å  
 251 across the entire structure, providing confidence that both enzymes shared a common structure and  
 252 function (**Fig. S15**). Both SQ monooxygenases consist of a core (α/β)<sub>8</sub> TIM barrel with three  
 253 additional insertion regions, analogous to monooxygenases from the bacterial luciferase family. The  
 254 protomers exist as a homodimer that buries 4697 Å<sup>2</sup> of surface area, amounting to 18% of total  
 255 accessible surface area for each protomer (**Fig. 3d**). Pairwise structural analysis using the DALI  
 256 server identified close relationships to a putative luciferase-like monooxygenase (3RAO.pdb) with  
 257 an rmsd of 2.4 over 314 residues and a Z score of 34.3, the FMNH<sub>2</sub>-dependent methanesulfonate  
 258 monooxygenase MsuD (7K14.pdb, rmsd 2.0/322 residues, Z-score of 41.0), and the FMNH<sub>2</sub>-  
 259 dependent alkanesulfonate monooxygenase SsuD (1M41.pdb, rmsd 1.8/317 residues, Z-score of  
 260 41.2).  
 261

262 Comparisons of the *RoSmoC* structure with MsuD (7K14.pdb) in complex with FMN enabled  
 263 identification of the FMN binding for site *RoSmoC*: a deep hydrophobic pocket that accommodates  
 264 the isoalloxazine ring system and extends out to the protein-solvent interface, which is gated by

265 conserved phosphate-binding residues Tyr136 and Ser189 (**Fig. 3e**) (18). The close structural and  
266 functional relationship of *RoSmoC* to *MsuD* is evident from the conservation of a putative sulfonate  
267 binding site comprised of the side-chains Trp206, Arg236, His238, Tyr341 and His343 (18). Aside  
268 from conferring these enzymes with an ability to bind sulfonates, these conserved active-site  
269 residues have been suggested to contribute to the stabilization of a peroxyflavin intermediate in  
270 *MsuD* and *SsuD* (18, 19). Efforts to obtain crystals of a *RoSmoC*–SQ complex were unsuccessful,  
271 limiting further insights into the origin of enzyme specificity towards SQ over other sulfonates.

272

### 273 *Atu3278 (smoB) encodes an oxidoreductase that converts 6-oxo-glucose to glucose*

274 *SmoB* is annotated as a short-chain dehydrogenase/reductase (SDR) and we had hypothesized that it  
275 was responsible for reduction of 6-OG to glucose (**Fig. 1d**). Since 6-OG is difficult to study  
276 directly, we tested our hypothesis by looking for *SmoB*-mediated isotope incorporation into glucose  
277 at equilibrium (**Fig. 4a**). Assuming our hypothesis to be true, and as a consequence of microscopic  
278 reversibility, incubation of *SmoB* with a nicotinamide co-factor and glucose in  $\text{H}_2^{18}\text{O}$  should result  
279 in transient formation of 6-OG, rapid and reversible hydration/dehydration with  $\text{H}_2^{18}\text{O}$  to compete-  
280 out  $^{16}\text{O}$  at C6 for  $^{18}\text{O}$ , and reduction to give 6- $^{18}\text{O}$ -glucose. In parallel to this process,  $^{18}\text{O}$   
281 incorporation will occur at C1 of glucose through a similar series of hydration/dehydration  
282 reactions. Before proceeding with these experiments, we used ITC to establish which nicotinamide  
283 cofactor was suitable for *SmoB*: NADPH bound to *SmoB* with  $K_d \sim 2 \mu\text{M}$ , while no binding was  
284 observed for NADH (**Fig. S16, Table S3**). Thus, glucose pre-equilibrated in  $\text{H}_2^{18}\text{O}$  was incubated  
285 with *SmoB* and  $\text{NADP}^+$  then analyzed by mass spectrometry to reveal the formation of a product 4  
286 Da greater in mass than glucose, presumably due to the incorporation of two  $^{18}\text{O}$  atoms into  
287 glucose. The crude reaction mixture was subjected to peracetylation ( $\text{Ac}_2\text{O}$ /pyridine) then LC-MS  
288 analysis to confirm that the +4 Da product co-eluted with authentic D-glucose-pentaacetate (**Fig.**  
289 **S17**). To determine that the  $^{18}\text{O}$  label was being incorporated at C6 of glucose, we used electron-  
290 impact GC-MS, which required conversion of the reaction product to the acyclic pentapropionate  
291 aldonitrile (**Fig. S18**) (20). This approach provided diagnostic C1-C5 and C5-C6 fragment ions. The  
292  $^{18}\text{O}$ -labelled product gave a C5-C6 fragment that was 2 mass units higher ( $m/z$  173 versus 175),  
293 whereas the C1-C5 fragment was the same as unlabelled glucose reference ( $m/z$  370),  
294 demonstrating that the  $^{18}\text{O}$  is incorporated at C6. Only enzymatic reactions conducted in the  
295 presence of  $\text{NADP}^+$  produced product labelled with  $^{18}\text{O}$  at C6:  $\text{NAD}^+$  failed to produce any product,  
296 supporting our observations by ITC and defining the cofactor specificity of *SmoB*.

297

298 We determined the 3D structure of *SmoB* using X-ray diffraction methods. This initial structure  
299 revealed that *SmoB* exists as a compact trimer, however the C-terminal His<sub>6</sub>-tag in this construct

300 occupied the putative active site of adjoining subunits, making co-crystallization with cofactors  
301 difficult (**Fig. S19**). To overcome this issue, SmoB was subcloned into a different vector and  
302 expressed with a cleavable N-terminal purification tag. This protein maintained the same catalytic  
303 activity and SEC-MALS confirmed it remained a trimer in solution (**Fig. S20**). This SmoB  
304 construct was co-crystallized with NADPH and a ternary product complex obtained by soaking  
305 crystals with D-glucose (**Fig. 4b**). These crystals diffracted to a resolution of 1.5 Å and the resulting  
306 model revealed that SmoB is an ( $\alpha/\beta$ )<sub>8</sub> TIM barrel fold with a C-terminal cofactor binding site. The  
307 overall fold has high structural conservation with members of the aldo-keto reductase (AKR)  
308 superfamily. SmoB binds NADPH with the 2'-phosphate oxygens hydrogen-bonded to Thr284,  
309 Arg289 and backbone amide of Asn285 and the adenine ring stacked between Arg289 and Phe241  
310 at the C-terminus (**Fig. 4c**). NADPH binds in an extended *anti*-conformation and the nicotinamide  
311 ring is located at the base of the substrate binding pocket. Trp232 makes a  $\pi$ - $\pi$  stacking interaction  
312 with the nicotinamide ring that positions the reactive center (C4) at a distance of 3 Å from C-6 of  
313 glucose, appropriate for hydride transfer (**Fig. 4d**). Within the SmoB•NADP<sup>+</sup>•glucose complex,  
314 glucose interacts with Arg152 (2.9 Å) and Lys120 (3 Å), as well as His151 (2.8 Å) and Tyr76 (2.7  
315 Å) within the conserved catalytic tetrad His/Tyr/Lys/Asp that is common to the AKR superfamily  
316 (**Fig. 4e**) (21).

317

### 318 *SMO pathways occur in the Alphaproteobacteria and Betaproteobacteria*

319 To ascertain how widespread this pathway for SQ utilization might be, a Multigene BLAST search  
320 was conducted of the non-redundant protein set of the NCBI for gene clusters that contain  
321 homologous SQases and SQ monooxygenases. This identified many putative *smo* gene clusters  
322 across the *Agrobacterium* and *Rhizobium* genus within the *Rhizobiales* order and evidence of some  
323 broader expansion into the Alphaproteobacteria and Betaproteobacteria classes (**Fig. 5**). Amongst  
324 these putative *smo* gene clusters, some were syntenic while others were substantially rearranged  
325 (non-syntenic) or modified to make use of other (non-ABC) transporter systems. The use of diverse  
326 transport systems is not surprising: a similar phenomenon has been observed for the tier-1 sulfo-ED  
327 pathway (5, 6). Indeed, sulfo-ED gene clusters have been identified in several *Rhizobiales* (5, 6),  
328 suggesting that there has been ample opportunity for genetic exchanges between these pathways  
329 during their evolution.

## **Discussion**

While existing pathways for the breakdown of SQ require two different organisms and involve scission of the carbon chain into two 3-carbon fragments, we describe here a fundamentally different approach that features complete utilization of the SQ carbon skeleton. The SMO pathway features several proteins with hitherto undescribed activities, including: an SQGro-binding protein; an FMNH<sub>2</sub>- and O<sub>2</sub>-dependent SQ monooxygenase that defines this ‘SMO’ pathway by catalyzing scission of the C–S bond in SQ; and an oxidoreductase dedicated to the NADPH-dependent reduction of 6-OG to glucose. Like all other sulfoglycolytic pathways studied to date, the SMO pathway also possesses a conserved SQase, which is essential for liberating SQ from its precursor glycoside SQGro (9, 10).

The SMO pathway is reminiscent of other sugar-metabolizing pathways in bacteria. For example, the SmoI (SQase), SmoF (SQGro binding protein) and SmoE/G/H (ABC transporter) proteins encoded by the *smo* cluster are analogous to MalP (maltodextrin phosphorylase), MalE (maltose binding protein) and MalF/G/K (ABC transporter) encoded by the *mal* operon of *E. coli* that imports and degrades maltose (22). Additionally, the SmoC (SQ monooxygenase) and SmoA (flavin reductase) proteins of the SMO pathway are reminiscent of the SsuD (FMNH<sub>2</sub>-dependent alkylsulfonate monooxygenase) and SsuE (NADPH-dependent FMN reductase) pair encoded by the *ssu* operon of *E. coli* that degrades alkanesulfonates (16). Indeed, it is likely that the SMO pathway arose through the recombination and neofunctionalization of analogous sugar- and sulfonate-metabolising pathways.

Through structural analysis we identified key residues involved in sulfosugar recognition and processing, in order to provide greater confidence to bioinformatic analyses of putative *smo* gene clusters: an approach that has proven valuable for the identification of tier 1 sulfoglycolytic pathways (9, 23, 24). This includes the Thr220-Gly166-Ser43-H<sub>2</sub>O(His13-Gln46) cluster of SmoF for the recognition of SQGro, the Arg283-Tryp286-H<sub>2</sub>O(Tyr491) triad of SmoI for the recognition of SQGro; and the Trp206-Arg236-His238-Tyr341-His343 constellation of SmoC for the recognition of SQ. Given the importance of the SQ monooxygenase SmoC to the SMO pathway, further empirical and computational work is warranted to understand what interactions drive its selectivity for SQ, which lies in contrast with the promiscuity exhibited by alkanesulfonate monooxygenases like SsuD.

The prevalence of the SMO pathway in Alphaproteobacteria of the *Rhizobiales* order is intriguing, since many bacteria of this order are plant symbionts or pathogens. Indeed, those bacteria that do

not possess an SMO pathway often possess a complementary tier 1 sulfo-ED pathway (5). Accordingly, it appears that plant sulfolipid catabolism is important for rhizobiales, whether they be plant pathogens/symbionts or free-living organisms adopting an oligotrophic saprophytic lifestyle in substrate replete with decaying plant tissues. Symbiotic bacteria of the *Rhizobiales* order reside within the root nodules of their plant host, where they harness four-carbon substrates from the host for energy and central metabolism (25). Sugawara and co-workers showed that sulfonate utilization gene clusters were expressed by the plant symbiont *Bradyrhizobium diazoefficiens* USDA 110 within these nodules and that this may be important for utilizing diverse sulfur sources to support symbiotic and possibly free-living lifestyles (26). With sulfolipid representing a large and accessible pool of sulfur in plants, one possible purpose of the SMO pathway may be to salvage sulfur for these bacteria. This is an important distinction between the SMO pathway and the tier 1 sulfoglycolytic pathways: the latter supports two-member microbial communities containing a second member with a tier 2 pathway to provide access to the sulfur of SQ (27). In this sense, use of the SMO pathway, which enables the complete utilization of the carbon skeleton and access to the sulfur of the monosaccharide can be considered a ‘selfish’ metabolic strategy, and could provide an advantage in the highly competitive soil environment or in the absence of other bacterial species within colonized plant tissues. Combined with the pathway’s requirement for molecular oxygen to effect C–S bond fissure, this may explain why the SMO pathway occurs within those bacteria that are commonly associated with plants. Understanding how the SMO and tier 1 pathways impact fitness within different environmental niches remains an important question, with answers that have significant implications for understanding plant diseases and symbioses, as well as soil chemistry.

## 387 **Methods**

### 388 *Specialist reagents*

389 SQ and methyl  $\alpha$ -sulfoquinovoside were purchased from MCAT GmbH (Donaueschingen,  
390 Germany), ( $^{13}\text{C}_6$ )SQ, glycer-1-yl  $\alpha$ -sulfoquinovoside (SQGro), and dicyclohexylammonium  
391 sulfolactate, cyclohexylammonium dihydroxypropanesulfonate were synthesized as described (13,  
392 28). All other sulfonates were purchased from Sigma-Aldrich.

393

### 394 *Growth studies*

395 Cultures of *A. tumefaciens* C58 were grown in a phosphate-buffered mineral salts media (M9, pH  
396 7.2), with glucose or SQ (10 mM) as the sole carbon source. Cultures were incubated at 30 °C (250  
397 rpm), with adaptation and robust growth observed within 2–3 days. These were sub-cultured (1%  
398 inoculum) into the same media (10 mL) and grown at 30 °C (250 rpm). Bacterial growth was  
399 quantitated using a Varian Cary50 UV/visible spectrophotometer to measure OD<sub>600</sub>. Growth  
400 experiments were replicated twice.

401

### 402 *Reducing sugar assay for culture supernatant*

403 The reducing sugar assay was performed according to the procedure of Blakeney and Mutton (29).  
404 This assay uses pre-prepared alkaline diluent and 4-hydroxybenzoic acid hydrazide (PAHBAH)  
405 working solution. Alkaline diluent was prepared by the addition of sodium hydroxide (20 g, 0.50  
406 mol) to a solution of 0.10 M trisodium citrate (50 mmol, 500 mL) and 0.02 M calcium chloride (13  
407 mmol, 500 mL). PAHBAH working solution was prepared by dissolving 4-hydroxybenzhydrazide  
408 (PAHBAH) (0.25 g, 1.6 mmol) in alkaline diluent (50 mL). The PAHBAH working solution should  
409 be made fresh shortly before use. To determine reducing sugar concentration, 0.90 mL of PAHBAH  
410 working solution was added to 0.10 mL of sample. The mixture was heated at 98 °C for 4 min then  
411 0.5 mL of the mixture was diluted into 1.0 mL of deionized water and the absorbance read at 415  
412 nm using a Varian Cary50 UV/visible spectrophotometer. Concentrations of SQ were determined  
413 with reference to a standard curve constructed using SQ.

414

### 415 *Turbidometric sulfate assay for culture supernatant*

416 The sulfate assay was performed according to the procedure of Sörbo (30). This assay uses a Ba-  
417 PEG reagent, which contains PEG to stabilize BaSO<sub>4</sub> crystals and a small amount of pre-formed  
418 BaSO<sub>4</sub> seed crystals to improve the reproducibility and linearity of the assay. The Ba-PEG reagent  
419 should be prepared fresh before use. Ba-PEG reagent was prepared by dissolving BaCl<sub>2</sub> (42 mg,  
420 0.20 mmol) and polyethylene glycol 6000 (0.75 g) in deionized water (5.0 mL). A small amount of  
421 Na<sub>2</sub>SO<sub>4</sub> (10  $\mu\text{L}$ , 50 mM) was added to this solution, with efficient magnetic stirring to generate

preformed BaSO<sub>4</sub> seed crystals. Individual sulfate assays were conducted as follows. An aliquot of culture supernatant obtained after pelleting of cells for 5 min at 5000 g (typically 100 µL, containing a maximum of 2.5 µmol of Na<sub>2</sub>SO<sub>4</sub>) was diluted to 0.1 mL with deionized water before the addition of 0.5 M HCl (0.1 mL) followed by Ba-PEG reagent (0.1 mL). The mixture was mixed vigorously and the absorbance of the sample at 400 nm determined using a Varian Cary50 UV/visible spectrophotometer. Concentrations of sulfate were determined by reference to a standard curve constructed using Na<sub>2</sub>SO<sub>4</sub>. This curve was linear up to 2.5 µmol of Na<sub>2</sub>SO<sub>4</sub>.

#### *Colorimetric fuchsin sulfite assay for culture supernatant*

The fuchsin sulfite assay was performed according to the procedures of Brychkova *et al.* (31) and Kurmanbayeva *et al.* (32). This procedure requires three pre-prepared solutions, Reagents A, B and C. Reagent A was prepared by dissolution of basic fuchsin (4.0 mg, 12 µmol) in deionized water (8.25 mL) at 0 °C, prior to the addition of 98% H<sub>2</sub>SO<sub>4</sub> (1.25 mL). Reagent B was prepared by diluting formaldehyde (36% in H<sub>2</sub>O, 0.32 mL) in deionized water (9.68 mL) at 0°C. Reagent C was prepared by dilution of Reagent A (1 mL) in deionized water (7 mL), prior to the addition of solution reagent B (1 mL). Individual sulfite assays were performed by addition of Reagent C (516 µL) to a mixture of sample (72 µL) and 0.5 mM Na<sub>2</sub>SO<sub>3</sub> (12 µL), with the latter providing a stable background signal for reference. The sample was incubated at 20-22°C for 10 min and the absorbance of the sample at 570 nm determined using a Varian Cary50 UV/visible spectrophotometer. Concentrations of sulfite were determined by reference to a standard curve constructed using Na<sub>2</sub>SO<sub>3</sub>.

#### *NMR analysis of metabolites produced from (<sup>13</sup>C<sub>6</sub>)SQ*

M9 minimal media (5 mL) containing 10 mM glucose was inoculated with *A. tumefaciens* C58 and grown to stationary phase at 30 °C (250 rpm). A 50 µL aliquot of this culture was used to inoculate 2 mL of M9 minimal media containing 10 mM (<sup>13</sup>C<sub>6</sub>)SQ and the culture incubated at 30 °C (250 rpm). At OD<sub>600</sub> 0.27 and OD<sub>600</sub> 0.49, 950 µL samples of culture supernatant were diluted with 100 µL of D<sub>2</sub>O and <sup>13</sup>C-NMR spectra acquired using a 400 MHz spectrophotomer (100 MHz for <sup>13</sup>C).

#### *Growth of A. tumefaciens C58 on diverse alkanesulfonates*

M9 minimal media (5 mL) containing 10 mM glucose was inoculated with *A. tumefaciens* C58 and grown to stationary phase at 30 °C (250 rpm). A 50 µL aliquot of this starter culture was used to inoculate 2 mL of M9 minimal media containing 10 mM of the alternative alkanesulfonate substrate: SQ (positive control), methyl α-sulfoquinovoside (MeSQ), glycer-1-yl α-sulfoquinovoside (SQGro), dicyclohexylammonium sulfolactate, cyclohexylammonium



457 dihydroxypropanesulfonate, sulfoacetic acid, taurine, sodium pentanesulfonate, cysteic acid,  
458 MOPS, HEPES, PIPES, MES and methanesulfonic acid. Cultures were incubated for 30 days at 30  
459 °C (250 rpm) with daily observations of optical density at 600 nm. Each experiment was performed  
460 in duplicate. Growth was observed on SQ (positive control), MeSQ, and SQGro, but not on any  
461 other sulfonate. Control experiments established that *A. tumefaciens* grows on glucose in the  
462 presence and absence of cyclohexylamine or dicyclohexylamine, and does not grow on  
463 cyclohexylamine or dicyclohexylamine alone.

464

#### 465 *Digestion of samples for quantitative proteomics*

466 Freeze dried *A. tumefaciens* whole-cell pellets were resuspend in 500 µL lysis buffer (4% SDS, 50  
467 mM Tris pH 8.5, 10 mM DTT) and boiled at 95 °C for 10 min with shaking at 2000 rpm to shear  
468 DNA and inactivate protease activity. Lysates were cooled to room temperature and protein  
469 concentration determined using a BCA assay. Each sample (200 µg of protein) was acetone  
470 precipitated by mixing 4 volumes of ice-cold acetone with one volume of sample. Samples were  
471 precipitated overnight at -20 °C and then centrifuged at 4000 × g for 10 min at 4 °C. The  
472 precipitated protein pellets were resuspended with 80% ice-cold acetone and precipitated for an  
473 additional 4 h at -20 °C. Samples were centrifuged at 17000 × g for 10 min at 4 °C to collect  
474 precipitated protein, the supernatant was discarded and excess acetone driven off at 65 °C for 5 min.  
475 Dried protein pellets were resuspended in 6 M urea, 2 M thiourea, 40 mM NH<sub>4</sub>HCO<sub>3</sub> and  
476 reduced/alkylated prior to digestion with Lys-C (1/200 w/w) then trypsin (1/50 w/w) overnight as  
477 previously described (33). Digested samples were acidified to a final concentration of 0.5% formic  
478 acid and desalted using C18 stage tips (34) before analysis by LC-MS.

479

#### 480 *Quantitative proteomics using reversed phase LC-MS*

481 Purified peptides were resuspended in Buffer A\* (2% MeCN, 0.1% TFA) and separated using a  
482 Proflow-equipped Dionex Ultimate 3000 Ultra-Performance Liquid Chromatography system  
483 (Thermo Fisher Scientific) with a two-column chromatography set up composed of a PepMap100  
484 C18 20 mm × 75 µm trap and a PepMap C18 500 mm × 75 µm analytical column (Thermo Fisher  
485 Scientific). Samples were concentrated onto the trap column at 5 µL min<sup>-1</sup> with Buffer A (2%  
486 MeCN, 0.1% FA) for 6 min and then infused into an Orbitrap Q-Exactive HF Mass Spectrometer  
487 (Thermo Fisher Scientific) at 250 nl min<sup>-1</sup>. Peptides were separated using 124-min gradients  
488 altering the buffer composition from 2% Buffer B (80% MeCN, 0.1% FA) to 8% B over 14 min,  
489 then from 8% B to 30% B over 80 min, 30% B to 45% B over 10 min, 45% B to 95% B over 2 min,  
490 holding at 95% B for 10, then dropped to 2% B over 1 min and holding at 2% B for the remaining 7  
491 min. The Q-Exactive HF™ Mass Spectrometer was operated in a data-dependent mode

492 automatically switching between the acquisition of a single Orbitrap MS scan (120,000 resolution)  
493 and a maximum of 20 MS-MS scans (HCD NCE 28, maximum fill time 40 ms, AGC  $2 \times 10^5$  with a  
494 resolution of 15,000).

495

#### 496 *Mass spectrometry data analysis*

497 Proteomics datasets were searched using MaxQuant (v1.5.3.3) (35) against the *A. tumefaciens* C58  
498 proteome (Uniprot proteome id UP000000813, downloaded 27/01/2018, 5344 entries). Searches  
499 were performed with carbamidomethylation of cysteine set as a fixed modification and oxidation of  
500 methionine as well as acetylation of protein N-termini allowed as variable modifications. The  
501 protease specificity was set to trypsin allowing 2 miscleavage events with a maximum false  
502 discovery rate (FDR) of 1.0% set for protein and peptide identifications. To enhance the  
503 identification of peptides between samples the Match Between Runs option was enabled with a  
504 precursor match window set to 2 min and an alignment window of 10 min. For label-free  
505 quantitation, the MaxLFQ option within Maxquant(36) was enabled in addition to the re-  
506 quantification module. The resulting protein group output was processed within the Perseus  
507 (v1.4.0.6) (37) analysis environment to remove reverse matches and common protein contaminants  
508 prior. For LFQ comparisons missing values were imputed using Perseus and Pearson correlations  
509 visualized using R. The mass spectrometry proteomics data have been deposited to the  
510 ProteomeXchange Consortium via the PRIDE (38) partner repository with the dataset identifier  
511 PXD014115.

512

#### 513 *Cloning*

514 Oligonucleotides encoding Atu3277 (SmoA), Atu3278 (SmoB), Atu3279 (SmoC) and Atu3282  
515 (SmoF) were amplified by PCR using Phusion polymerase HF master mix (NEB), the appropriate  
516 primers listed in **Table S1** and *A. tumefaciens* C58 gDNA as template. Oligonucleotides encoding  
517 RoSmoA and RoSmoC were synthesized (IDT) to provide the sequences listed in **Table S1**. These  
518 were cloned into the pET29b(+) vector at the *NdeI* and *XhoI* sites and sequence-verified by Sanger  
519 sequencing to give expression vectors for SmoA, SmoB, SmoC, SmoF, RoSmoA and RoSmoC.  
520 Due to interference from the SmoB C-terminal His<sub>6</sub>-tag during structural studies, the *smoB*  
521 (*Atu3278*) gene was sub-cloned into the pET-YSBLIC3C vector (39) by PCR amplification with the  
522 relevant primers in **Table S1** and In-Fusion<sup>®</sup> cloning (Clontech Laboratories, Inc.) into linearized  
523 YSBLIC3C vector according to the manufacturer's protocol. The expression plasmid was sequence-  
524 verified by Sanger sequencing.

525

#### 526 *Protein expression and purification*

527 All vectors were transformed into 'T7 Express' *E. coli* (NEB), except for the vector encoding SmoF  
528 (Atu3282), which was transformed into 'Shuffle<sup>®</sup> T7' *E. coli* (NEB), and all were plated onto LB-  
529 agar (50  $\mu\text{g mL}^{-1}$  kanamycin) and incubated at 37 °C for 16 h. A single colony was used to  
530 inoculate 10 mL of LB media containing 50  $\mu\text{g mL}^{-1}$  kanamycin and the cultures incubated at 37 °C  
531 for 16 h. These starter cultures were used to inoculate 1000 mL of S-broth (35 g tryptone, 20 g yeast  
532 extract, 5 g NaCl, pH 7.4) containing 50  $\mu\text{g mL}^{-1}$  kanamycin, which was incubated with shaking  
533 (250 rpm) at 37 °C until it reached an OD<sub>600</sub> of 0.8. Each culture was cooled to room temperature,  
534 isopropyl thiogalactoside (IPTG) added to a final concentration of 400  $\mu\text{M}$ , and incubation with  
535 shaking (200 rpm) continued at 18 °C for 19 h. Cells were harvested by centrifugation at 8,000 g for  
536 20 min at 4 °C then resuspended in 40 mL binding buffer (50 mM NaPi, 300 mM NaCl, 5 mM  
537 imidazole, pH 7.5) containing protease inhibitor (Roche cOmplete EDTA-free protease inhibitor  
538 cocktail) and lysozyme (0.1 mg mL<sup>-1</sup>) by nutating at 4 °C for 30 min. Benzonase (1  $\mu\text{L}$ , 250 U) was  
539 added to the mixture then lysis was effected by sonication [10 $\times$  (15 s on / 45 s off) at 45%  
540 amplitude]. The lysate was centrifuged at 18,000 g for 20 min at 4 °C and the supernatant collected.  
541 The supernatants were filtered (0.45  $\mu\text{m}$ ) and loaded onto a 1 mL HiTrap TALON IMAC column  
542 (GE). The column was washed with 3  $\times$  10 mL of binding buffer, then the protein was eluted using  
543 elution buffer (50 mM NaPi, 300 mM NaCl, 400 mM imidazole, pH 7.5). Fractions containing  
544 product, as judged by SDS-PAGE, were further purified by size exclusion chromatography on a  
545 HiPrep 16/60 Sephacryl S-200 HR column (GE) using 50 mM NaPi, 150 mM NaCl, pH 7.5  
546 (Atu3277 SmoA; Atu3278, SmoB; Atu3279, SmoC) or 50 mM sodium citrate, 150 mM NaCl, pH  
547 5.5 (Atu3282, SmoF) as buffer (**Fig. S2**). SmoI (Atu3285 or AtSQase) was prepared as previously  
548 described (9).

549

#### 550 *SEC-MALS analyses*

551 Experiments were conducted on a system comprising a Wyatt HELEOS-II multi-angle light  
552 scattering detector and a Wyatt rEX refractive index detector linked to a Shimadzu LC system  
553 (SPD-20A UV detector, LC20-AD isocratic pump system, DGU-20A3 degasser and SIL-20A  
554 autosampler). Experiments were conducted at room temperature (20  $\pm$  2°C). Solvents were filtered  
555 through a 0.2  $\mu\text{m}$  filter prior to use and a 0.1  $\mu\text{m}$  filter was present in the flow path. The column  
556 was equilibrated with > 2 CV of buffer (50 mM NaPi, 300 mM NaCl pH 7.4) before use and buffer  
557 was infused at the working flow rate until baselines for UV, light scattering and refractive index  
558 detectors were all stable. The sample injection volume was 100  $\mu\text{L}$  of protein at 6 mg mL<sup>-1</sup> in 50  
559 mM NaPi buffer, 300 mM NaCl pH 7.4. Shimadzu LC Solutions software was used to control the  
560 LC and Astra V software for the HELEOS-II and rEX detectors. The Astra data collection was 1  
561 min shorter than the LC solutions run to maintain synchronization. Blank buffer injections were

562 used as appropriate to check for carry-over between sample runs. Data were analyzed using the  
563 Astra V software. Molecular weights were estimated using the Zimm fit method with degree 1. A  
564 value of 0.158 was used for protein refractive index increment (dn/dc).

565

#### 566 *Isothermal Titration Calorimetry*

567 ITC experiments were performed using a MicroCal iTC200 (GE Healthcare) at 25 °C, with a 750  
568 r.p.m. stirring speed and a reference power of 10  $\mu\text{Cal.s}^{-1}$ . Proteins and substrates were equilibrated  
569 into degassed and filter-sterilized buffer (50 mM NaPi, 200 mM NaCl, pH 7.4 for SmoC/F and 25  
570 mM NaPi, pH 7.5 for Smo B). Protein concentration was determined by BCA assay (Thermo  
571 Fisher) before initiating experiments. For SmoC–SQ binding, 600  $\mu\text{M}$  SQ was titrated into the ITC  
572 cell containing 40  $\mu\text{M}$  SmoC as a series of  $10 \times 3.94 \mu\text{L}$  injections with a pre-injection of  $1 \times 0.4$   
573  $\mu\text{L}$ . For SmoF–SQGro binding, 200  $\mu\text{M}$  SQGro was titrated into the ITC cell containing 20  $\mu\text{M}$   
574 SmoF as a series of  $15 \times 2.94 \mu\text{L}$  injections with a pre-injection of  $1 \times 0.4 \mu\text{L}$ . The delay between  
575 injections was set at 120 s, with an initial injection delay of 60 s. For SmoB–NAD(P)H binding, 1  
576 mM NADH was titrated into the ITC cell containing 40  $\mu\text{M}$  SmoB as a series of  $19 \times 3 \mu\text{L}$   
577 injections with a pre-injection of  $1 \times 4 \mu\text{L}$ . The delay between injections was set at 150 s, with an  
578 initial injection delay of 180 s. All data analysis was performed in MicroCal ITC Origin Analysis  
579 software (Malvern).

580

#### 581 *Nano Differential Scanning Fluorescence analysis of SmoF*

582 Thermal stability analysis for SmoF in the presence and absence of SQGro ligand was performed on  
583 a Prometheus NT.48 (NanoTemper) at 15% excitation, scanning from 20 °C to 65 °C at 0.5 °C min<sup>-1</sup>.  
584 All protein samples were at a concentration of 1 mg mL<sup>-1</sup> in 50 mM citrate, 150 mM NaCl at pH  
585 5.5, with a 10  $\mu\text{L}$  capillary load per sample. Data acquisition and analysis was performed with  
586 PR.ThermControl (NanoTemper) software.

587

#### 588 *Identification of the flavin co-factor that co-purified with SmoA*

589 100  $\mu\text{L}$  of recombinant flavin reductase (SmoA or RoSmoA) at a concentration of 20 mg mL<sup>-1</sup> in 50  
590 mM Tris, 150 mM NaCl, pH 8.5 was heated at 90 °C for 10 min. The sample was clarified by  
591 centrifugation (16,000  $\times g$ , 10 min, 4 °C) and the supernatant filtered (0.2  $\mu\text{m}$ ). Samples were  
592 analyzed by LCMS on an Agilent LCMS system (G6125B mass detector, 1290 Infinity G7120A  
593 high speed pump, 1290 Infinity G7129B autosampler, and 1290 Infinity G7117B diode array  
594 detector). Conditions for LC were as follows: column: Phenomenex 00B-4752-AN Luna Omega 1.6  
595  $\mu\text{m}$  PS C<sub>18</sub> 100Å (50  $\times$  2.1 mm); injection volume: 1  $\mu\text{L}$ ; gradient: 3 to 100% B over 20 min

(solvent A: water + 0.1% FA; solvent B: MeCN + 0.1% FA); flow rate: 0.6 mL min<sup>-1</sup>; DAD – 254 and 214 nm.

#### *Michaelis-Menten kinetic analyses of SmoA and RoSmoA*

Reactions were conducted at 25 °C in 96-well plate format and involved the addition of SmoA or RoSmoA (final concentration of 20 nM for NADH and 500 nM for NADPH) to 20–800 μM NAD(P)H in 50 mM NaPi, 150 mM NaCl, 30 μM FMN, 0.01% BSA, pH 7.4 at a total volume of 100 μL. The progress of the enzyme-catalyzed conversion of NAD(P)H to NAD(P)<sup>+</sup> was monitored by measuring loss of absorbance at 340 nM over time using an Envision Multimodal Plate Reader (Perkin Elmer). Initial rates for each reaction were calculated after first subtracting the rate of spontaneous NAD(P)H oxidation (determined using an enzyme-free control) and an empirically determined extinction coefficient for NAD(P)H under these conditions. Each initial rate was determined in triplicate and fit to a Michaelis-Menten equation using Prism 8 (GraphPad).

#### *Sulfoquinovose monooxygenase assay*

This SQ monooxygenase activity assay is based on a previously described alkanesulfonate monooxygenase activity assays (19) and uses Ellman's reagent to quantify sulfite released by these enzymes. A 2 mL reaction containing 1 mM SQ, 1 mM NADH, 3 μM FMN, 0.01% (w/v) BSA, 100 nM SmoA or RoSmoA and 300 nM SQ monooxygenase (SmoC or RoSmoC) in buffer (25 mM Tris pH 9.1, 25 mM NaCl) was incubated at 30 °C, along with controls lacking reaction components or using alternate sulfonate substrates. Reactions were initiated by the addition of SmoA or RoSmoA to the mixture. Sulfite concentration in the samples was determined at discrete time points by quenching 40 μL of the reaction in 160 μL of Ellman's reagent (0.125 mg mL<sup>-1</sup> in 25 mM NaPi pH 7.0, prepared fresh) within a 96-well plate. After 60 s, the absorbance of the sample at 405 nm was determined using an Envision Multimodal Plate Reader (Perkin Elmer). The sulfite concentration was interpolated using a calibration curve generated under these conditions: a linear relationship between sulfite concentration and absorbance at 405 nm was observed for 5–1000 μM Na<sub>2</sub>SO<sub>3</sub>. The activity of SQ monooxygenases at different pH was determined by modifying the buffer in the above reactions (MES: pH 6.0, 6.5 and Tris: pH 7.0, 7.5, 8.0, 8.5, 9.1) using an endpoint of *t* = 30 min.

#### *Equilibrium isotope labelling using SmoB*

In order to pre-label the anomeric position, glucose was incubated in 98% H<sub>2</sub><sup>18</sup>O with heating at 80 °C for 2 days, then evaporated to dryness to give C1-<sup>18</sup>O-labelled glucose. Labelling was determined to be 95% by mass spectrometry based on intensities of the M and M+2 peaks. Using H<sub>2</sub><sup>18</sup>O buffer

(100 mM potassium phosphate, pH 7.0),  $\text{NAD}^+$  and  $\text{NADP}^+$  were each added at 0.05 molar equivalent to C1- $^{18}\text{O}$ -glucose and SmoB. Four control experiments were conducted: one without enzyme, one without  $\text{NAD}^+$  and  $\text{NADP}^+$ , one in  $\text{H}_2^{16}\text{O}$ , and one in  $\text{H}_2^{16}\text{O}$  with unlabeled glucose. Reactions were monitored by mass spectrometry. Only in the experimental sample containing enzyme,  $\text{H}_2^{18}\text{O}$  and  $\text{NAD}^+/\text{NADP}^+$  was an M+4 signal observed and this reached a maximum intensity after 72 h. Two additional reactions were performed using SmoB, glucose and either  $\text{NADP}^+$  or  $\text{NAD}^+$  in  $\text{H}_2^{18}\text{O}$  and only the reaction containing  $\text{NADP}^+$  generated the M+4 species. To confirm that the M+4 species was glucose with two  $^{18}\text{O}$  labels, we studied the product by HPLC. However, under aqueous HPLC conditions the  $^{18}\text{O}$ -label at C1 is lost through chemical exchange with solvent. Therefore, we acetylated the product to form the pentaacetate to ensure no exchange at the anomeric position during HPLC analysis. The reaction mixture from above was evaporated under reduced pressure. The crude residue was treated with acetic anhydride in pyridine (1:2, 1 mL) overnight. The product was extracted with EtOAc and washed with sat.  $\text{CuSO}_4$  to remove pyridine. The organic solution containing peracetylated glucose was analyzed by LCMS on an Agilent LCMS system (G6125B mass detector, 1290 Infinity G7120A high speed pump, 1290 Infinity G7129B autosampler, and 1290 Infinity G7117B diode array detector). Conditions for LC were as follows: column: Phenomenex 00B-4752-AN Luna Omega 1.6  $\mu\text{m}$  PS  $\text{C}_{18}$  100Å (50  $\times$  2.1 mm); injection volume: 1  $\mu\text{L}$ ; gradient: 0 to 65% B over 20 min (solvent A: water + 0.1% FA; solvent B: MeCN + 0.1% FA); flow rate: 0.6  $\text{mL min}^{-1}$ . Peaks with  $m/z$  413  $[\text{M}+\text{Na}]^+$ ,  $m/z$  415  $[\text{M}+2+\text{Na}]^+$ , and  $m/z$  417  $[\text{M}+4+\text{Na}]^+$  had the same retention time as an authentic glucose pentaacetate standard.

651

#### 652 GC-MS analysis of isotopically-labelled carbohydrates

653 A 0.1  $\mu\text{L}$  aliquot of SmoB-glucose reaction mixture (containing  $\approx 2.5$  nmol glucose) was transferred  
654 to a GC vial insert (deactivated) together with 1 nmol *scyllo*-inositol as an internal standard.  
655 Samples were derivatized as described in Antoniewicz *et al.* (20), with minor modifications.  
656 Briefly, samples were dried (*in vacuo*, 35  $^\circ\text{C}$  with a 40  $\mu\text{L}$  methanol wash), followed by addition of  
657 hydroxylamine hydrochloride (20  $\text{mg mL}^{-1}$  in 25  $\mu\text{L}$  pyridine) and incubation at 90  $^\circ\text{C}$  for 1 h. Vials  
658 were cooled briefly at 20-22 $^\circ\text{C}$  before the addition of propionic anhydride (50  $\mu\text{L}$ ) and incubation at  
659 60  $^\circ\text{C}$  for 30 min. Samples were evaporated to dryness under a stream of nitrogen at 60  $^\circ\text{C}$  and  
660 resuspended in EtOAc (40  $\mu\text{L}$ ). Control samples of U- $^{12}\text{C}$ -glucose, U- $^{13}\text{C}$ -glucose, 1,2- $^{13}\text{C}_2$ -glucose  
661 and 6,6- $^2\text{H}_2$ -glucose were also prepared at a 2.5 nmol scale in the assay buffer mixture. Samples  
662 were blinded for analysis. The derivatized labelled glucose samples (**Fig. S13** and **Table S7**) were  
663 analyzed by GC-MS using a DB5 capillary column (J&W Scientific, 30 m, 250  $\mu\text{m}$  inner diameter,  
664 0.25  $\mu\text{m}$  film thickness) with a 10 m inert duraguard. The injector insert and GC-MS transfer line  
665 temperatures were 270  $^\circ\text{C}$  and 250  $^\circ\text{C}$ , respectively. The oven temperature gradient was

666 programmed as follows: 70 °C (1 min); 70 °C to 295 °C at 12.5 °C min<sup>-1</sup>; 295 °C to 320 °C at 25 °C  
667 min<sup>-1</sup>; 320 °C for 2 min. Glucose and *scyllo*-inositol were identified by reference to authentic  
668 standards. A calibration curve was generated using glucose standard in assay buffer (starting  
669 concentration 50 nmol, 2-fold dilution series). **Fig. S12** shows the fraction of labelled fragments,  
670 corrected for isotope natural abundance by DExSI analysis (40).

671

#### 672 *Protein crystallization*

673 Initial crystallization screening was performed using commercially available INDEX (Hampton  
674 Research), PACT premier and CSSI/II (Molecular Dimensions) screens in 96-well sitting drop  
675 trays. Further optimization was carried out in a 48-well sitting drop or 24-well hanging-drop format  
676 to obtain optimal crystals for X-ray diffraction. Unless otherwise stated, all crystals were grown at  
677 20 °C.

678

679 Crystals of apo-SmoF were obtained by mixing 0.15 µL of protein stock (50 mg mL<sup>-1</sup> protein in 50  
680 mM citrate, 150 mM NaCl, pH 5.5) with 0.15 µL mother liquor (0.3 M ammonium acetate, 0.1 M  
681 Bis-Tris, 25% w/v PEG 3350, pH 5.5) housed in a Rigaku Xtaltrak plate hotel to enable consistent  
682 growth and monitoring at 6 °C. Crystals were harvested with nylon CryoLoops<sup>TM</sup> (Hampton  
683 Research) and cryopreserved in liquid nitrogen without additional cryoprotectants.

684

685 Crystals of SmoF were initially obtained by mixing 0.15 µL of protein stock (3.5 mg mL<sup>-1</sup> protein  
686 with 2'R-SQGro at a 1:10 molar ratio in 50 mM citrate, 150 mM NaCl, pH 5.5) with 0.15 µL  
687 mother liquor (30% (w/v) polyethylene glycol 4000, 0.2 M sodium acetate, 0.1 M tris chloride, pH  
688 8.5). The resulting crystals were used to prepare a seed stock by mixing the crystallization drop  
689 with 100 µL mother liquor and vortexing for 60 s with one teflon bead. An optimisation plate was  
690 setup with drops comprised of 0.1 µl of various mother liquors (28-36% (w/v) polyethylene glycol  
691 4000, 0.2 M sodium acetate, 0.1 M tris chloride, pH 7.1-9.1), 50 nl seed stock solution, and 0.15 µL  
692 protein stock (4 mg mL<sup>-1</sup> protein with 2'R-SQGro at a 1:10 molar ratio in 50 mM citrate, 150 mM  
693 NaCl, pH 5.5). A single crystal grown at 31.8% (w/v) polyethylene glycol 4000, 0.2 M sodium  
694 acetate, 0.1 M tris chloride, pH 8.95, was harvested with a nylon CryoLoop<sup>TM</sup> (Hampton Research)  
695 and cryopreserved in liquid nitrogen with 25% (v/v) ethylene glycol as cryoprotectant.

696

697 Crystals of SmoI-D455N-E370A-E371A were obtained by mixing 0.4 µL of protein stock (35 mg  
698 mL<sup>-1</sup> protein in 50 mM NaPi, 300 mM NaCl, pH 7.4) with 0.5 µL mother liquor (26% PEG 3350  
699 w/v, 0.2 M KSCN, 0.1 M Bis-Tris propane, pH 6.5). Crystals were soaked with solid SQGro in

700 mother liquor for 2 min prior to harvesting with nylon CryoLoops<sup>TM</sup> (Hampton Research) and  
701 cryopreserved without additional cryoprotectants.

702

703 Crystals of apo-SmoC were obtained by mixing 0.6  $\mu$ L of protein stock (60 mg mL<sup>-1</sup> protein in 50  
704 mM Tris, 300 mM NaCl, pH 7.5) with 0.5  $\mu$ L mother liquor (0.2 M NaCl, 0.1 M MES pH 6, 26%  
705 PEG 6000 w/v and 10 mM SQ-glucitol). Crystals of apo-RoSmoC were obtained by mixing 0.1  $\mu$ L  
706 of protein stock (11.7 mg mL<sup>-1</sup> protein in 50 mM Tris, 300 mM NaCl, pH 7.5) with 0.2  $\mu$ L mother  
707 liquor (0.2M NaNO<sub>3</sub>, 20% PEG 3350 w/v and 10 mM SQ). Crystals were harvested with nylon  
708 CryoLoops<sup>TM</sup> (Hampton Research) and cryopreserved in liquid nitrogen without additional  
709 cryoprotectants.

710

711 Crystals of SmoB-apo (YSBLIC3C construct) were obtained by mixing 0.15  $\mu$ L of protein stock  
712 (20 mg mL<sup>-1</sup> protein in 50 mM NaPi, 150 mM NaCl, pH 7.4) with 0.15  $\mu$ L mother liquor (0.2 M  
713 sodium malonate dibasic monohydrate, 0.1 M Bis-Tris propane pH 8.5, 20% w/v PEG 3350). For  
714 the SmoB•NADPH complex, crystals were obtained by mixing 0.15  $\mu$ L of protein stock (20 mg  
715 mL<sup>-1</sup> protein in 50 mM NaPi, 150 mM NaCl, 2 mM NADPH, pH 7.4) with 0.15  $\mu$ L mother liquor  
716 (0.1 M succinic acid, sodium dihydrogen phosphate, glycine buffer (SPG buffer, Qiagen), 25% w/v  
717 PEG 1500 at pH 6.0). For the SmoB•NADPH•Glc complex, crystals were obtained in a hanging  
718 drop by mixing 1  $\mu$ L of protein stock (13 mg mL<sup>-1</sup> protein in 50 mM NaPi 150 mM NaCl, pH 7.4)  
719 with 1  $\mu$ L of mother liquor (2 mM NADPH, 0.1 M SPG (Qiagen), 25% w/v PEG 1500 at pH 6).  
720 Crystals were soaked with solid glucose in mother liquor for 1 min prior to harvesting with nylon  
721 CryoLoops<sup>TM</sup> (Hampton Research) and cryopreserved without additional cryoprotectants.

722

### 723 *X-ray data collection, processing and refinement*

724 The data were processed and integrated using XDS (41) and scaled using SCALA (42) included in  
725 the Xia2 processing system (43). Data reduction was performed with AIMLESS, and resolution was  
726 cut until CC1/2 = 0.5. The structure of the SmoI•SQGro complex was determined using molecular  
727 replacement using 5OHS (9) as the initial model. For SmoF, the structure was solved by molecular  
728 replacement using PHASER (44) with a search model created from PDB ID: 6DTQ (45). The  
729 structure of RoSmoC was solved by molecular replacement using the ensemble based on PDB ID:  
730 1M41 (19) as an initial search model. The structure of SmoB was determined using molecular  
731 replacement with the monomer of an aldo-keto reductase from *S. enterica* (PDB ID: 4R9O) as the  
732 initial model. The apo-SmoF structure was solved using a dissected C-terminal domain of the  
733 SmoF•SQGro structure. Structures were built and refined by iterative cycles using Coot (46) and  
734 REFMAC (47) or Phenix (48), the latter employing local NCS restraints. Following building and



refinement of the protein and water molecules, clear residual density was observed in the omit maps for co-complex structures, respective ligands were modelled into these. The coordinate and refinement library files were prepared using ACEDRG (49). The final structures gave  $R_{\text{cryst}}$  and  $R_{\text{free}}$  values along with data and refinement statistics that are presented in **Table S4-6**. Data were collected at Diamond light source, Didcot, Oxfordshire, U.K., on beamlines I24 (SmoI-D455N•SQGro, to 2.15 Å; SmoF-apo, to 1.88 Å), I04 (RoSmoC to 1.75 Å) and I04-1 (SmoC-apo, to 3.2 Å; SmoB-apo\_YSBLIC3C, to 1.5 Å; SmoB-apo; pET29a; SmoB•NADPH and SmoB•NADPH•Glc) and at the Australian Synchrotron using the MX2 beamline (At3282•SQGro complex, to 1.7 Å). The coordinate files and structure factors have been deposited in the Protein DataBank (PDB) with the coordinate accession numbers 7OFX (SmoI-D455N•SQGro), 7NBZ (SmoF-apo), 7OFY (SmoF•SQGro), 7OH2 (RoSmoC), 7OLF (SmoC-apo), 7BBY (SmoB-apo; pET29a), 7BBZ (SmoB-apo; YSBLIC3C), 7BC0 (SmoB•NADPH) and 7BC1 (SmoB•NADPH•Glc).

748

#### 749 *Structure-based analyses*

Crystal packing interactions were analyzed using the protein interactions, surfaces, and assemblies (PISA) server (50). Structural comparisons and structure-based sequence alignments were conducted using PDB25 search on DALI server against a representative subset of the Protein Data Bank (51). All structure figures were generated using ccp4mg (52).

754

#### 755 *Bioinformatic analysis SMO pathway prevalence*

Each gene within the *A. tumefaciens* C58 SMO gene cluster (*Atu3277-Atu3285*) was submitted as a query to the NCBI BLASTp algorithm to search a database comprised of non-redundant protein sequences with *A. tumefaciens* (taxid: 358) sequences excluded. Standard algorithm parameters were used, except the maximum target sequences was set to 10,000. Results were filtered to only retain protein sequences with E-value  $\leq 1.19 \times 10^{-51}$ . The corresponding nucleotide accession numbers for each protein from all nine searches were extracted, combined and duplicates removed to provide a list of candidate genome sequences. This was converted into a reference library for MultiGeneBLAST (53) and queried using the *A. tumefaciens* C58 SMO gene cluster. Clusters identified by this workflow with both an SQ monooxygenase and SQase homolog were regarded as putative SMO gene clusters. Clusters representative of the observed diversity were visualized using Clinker (54). A phylogenetic tree of species possessing a putative SMO gene cluster was generated by pruning the All-Species Living Tree Project's 16s rRNA release 132 (55) using iTOL (56).

768

#### 769 **Data Availability Statement**

770 Structure coordinates have been deposited in the Protein Data Bank (<https://www.rcsb.org/>) under  
771 accession codes 7OFX, 7OFY, 7NBZ, 7OH2, 7OLF, 7BBZ, 7BC0, 7BC1 and 7BBY. Proteomics  
772 data are available via ProteomeXchange (57) (<http://www.proteomexchange.org/>) with the identifier  
773 PXD014115. Scripts used to screen for the related gene clusters listed in Figure 5 is available on  
774 GitHub (<https://github.com/jmui-unimelb/Gene-Cluster-Search-Pipeline>).

775

- 777 1. E. D. Goddard-Borger, S. J. Williams Sulfoquinovose in the biosphere: occurrence,  
778 metabolism and functions. *Biochem. J.* **474**, 827–849 (2017).
- 779 2. J. L. Harwood, R. G. Nicholls The plant sulpholipid - a major component of the sulphur  
780 cycle. *Biochem. Soc. Trans.* **7**, 440-447 (1979).
- 781 3. N. Mizusawa, H. Wada The role of lipids in photosystem II. *Biochim. Biophys. Acta* **1817**,  
782 194-208 (2012).
- 783 4. K. Denger, *et al.* Sulphoglycolysis in *Escherichia coli* K-12 closes a gap in the  
784 biogeochemical sulphur cycle. *Nature* **507**, 114-117 (2014).
- 785 5. A. K. Felux, D. Spiteller, J. Klebensberger, D. Schleheck Entner-Doudoroff pathway for  
786 sulfoquinovose degradation in *Pseudomonas putida* SQ1. *Proc. Natl. Acad. Sci. USA* **112**,  
787 E4298-4305 (2015).
- 788 6. J. Li, *et al.* A Sulfoglycolytic Entner-Doudoroff Pathway in *Rhizobium leguminosarum* bv.  
789 *trifolii* SRDI565. *Appl. Environ. Microbiol.* **86**, e00750-00720 (2020).
- 790 7. B. Frommeyer, *et al.* Environmental and Intestinal Phylum Firmicutes Bacteria Metabolize  
791 the Plant Sugar Sulfoquinovose via a 6-Deoxy-6-sulfofructose Transaldolase Pathway.  
792 *iScience* **23**, 101510 (2020).
- 793 8. Y. Liu, *et al.* A transaldolase-dependent sulfoglycolysis pathway in *Bacillus megaterium*  
794 DSM 1804. *Biochem. Biophys. Res. Commun.* **533**, 1109-1114 (2020).
- 795 9. P. Abayakoon, *et al.* Structural and Biochemical Insights into the Function and Evolution of  
796 Sulfoquinovosidases. *ACS Cent. Sci.* **4**, 1266-1273 (2018).
- 797 10. G. Speciale, Y. Jin, G. J. Davies, S. J. Williams, E. D. Goddard-Borger YihQ is a  
798 sulfoquinovosidase that cleaves sulfoquinovosyl diacylglyceride sulfolipids. *Nat. Chem.*  
799 *Biol.* **12**, 215-217 (2016).
- 800 11. A. B. Roy, M. J. Hewlins, A. J. Ellis, J. L. Harwood, G. F. White Glycolytic breakdown of  
801 sulfoquinovose in bacteria: a missing link in the sulfur cycle. *Appl. Environ. Microbiol.* **69**,  
802 6434-6441 (2003).
- 803 12. M. A. Kertesz Riding the sulfur cycle - metabolism of sulfonates and sulfate esters in Gram-  
804 negative bacteria. *FEMS Microbiol. Rev.* **24**, 135-175 (2000).
- 805 13. P. Abayakoon, *et al.* Comprehensive synthesis of substrates, intermediates and products of  
806 the sulfoglycolytic Embden-Meyerhoff-Parnas pathway. *J. Org. Chem.* **84**, 2901-2910  
807 (2019).
- 808 14. A. E. Speers, C. C. Wu Proteomics of Integral Membrane Proteins: Theory and Application.  
809 *Chem. Rev.* **107**, 3687-3714 (2007).
- 810 15. A. L. Davidson, E. Dassa, C. Orelle, J. Chen Structure, Function, and Evolution of Bacterial  
811 ATP-Binding Cassette Systems. *Microbiol. Mol. Biol. Rev.* **72**, 317-364 (2008).
- 812 16. J. R. van Der Ploeg, R. Iwanicka-Nowicka, T. Bykowski, M. M. Hryniewicz, T. Leisinger  
813 The *Escherichia coli* ssuEADCB gene cluster is required for the utilization of sulfur from  
814 aliphatic sulfonates and is regulated by the transcriptional activator Cbl. *J. Biol. Chem.* **274**,  
815 29358-29365 (1999).
- 816 17. A. Thakur, *et al.* Substrate-Dependent Mobile Loop Conformational Changes in  
817 Alkanesulfonate Monooxygenase from Accelerated Molecular Dynamics. *Biochemistry* **59**,  
818 3582-3593 (2020).
- 819 18. J. J. M. Liew, I. M. El Saudi, S. V. Nguyen, D. K. Wicht, D. P. Dowling Structures of the  
820 alkanesulfonate monooxygenase MsuD provide insight into C-S bond cleavage, substrate  
821 scope, and an unexpected role for the tetramer. *J. Biol. Chem.* **297**, (2021).
- 822 19. E. Eichhorn, C. A. Davey, D. F. Sargent, T. Leisinger, T. J. Richmond Crystal Structure of  
823 *Escherichia coli* Alkanesulfonate Monooxygenase SsuD. *J. Mol. Biol.* **324**, 457-468 (2002).
- 824 20. M. R. Antoniewicz, J. K. Kelleher, G. Stephanopoulos Measuring deuterium enrichment of  
825 glucose hydrogen atoms by gas chromatography/mass spectrometry. *Anal. Chem.* **83**, 3211-  
826 3216 (2011).

- 827 21. T. M. Penning The aldo-keto reductases (AKRs): Overview. *Chem. Biol. Interact.* **234**, 236-  
828 246 (2015).
- 829 22. R. Dippel, W. Boos The Maltodextrin System of *Escherichia coli*: Metabolism and  
830 Transport. *J. Bacteriol.* **187**, 8322 (2005).
- 831 23. M. Sharma, *et al.* Dynamic Structural Changes Accompany the Production of  
832 Dihydroxypropanesulfonate by Sulfolactaldehyde Reductase. *ACS Catalysis* **10**, 2826-2836  
833 (2020).
- 834 24. M. Sharma, *et al.* Molecular Basis of Sulfosugar Selectivity in Sulfoglycolysis. *ACS Cent.*  
835 *Sci.* **7**, 476-487 (2021).
- 836 25. M. Udvardi, P. S. Poole Transport and metabolism in legume-rhizobia symbioses. *Annu.*  
837 *Rev. Plant Biol.* **64**, 781-805 (2013).
- 838 26. J. J. Speck, E. K. James, M. Sugawara, M. J. Sadowsky, P. Gyaneshwar An Alkane  
839 Sulfonate Monooxygenase Is Required for Symbiotic Nitrogen Fixation by *Bradyrhizobium*  
840 *diazoefficiens* (syn. *Bradyrhizobium japonicum*) USDA110(T). *Appl. Environ. Microbiol.*  
841 **85**, (2019).
- 842 27. K. Denger, T. Huhn, K. Hollemeyer, D. Schleheck, A. M. Cook Sulfoquinovose degraded  
843 by pure cultures of bacteria with release of C<sub>3</sub>-organosulfonates: complete degradation in  
844 two-member communities. *FEMS Microbiol. Lett.* **328**, 39-45 (2012).
- 845 28. Y. Zhang, *et al.* Concise synthesis of sulfoquinovose and sulfoquinovosyl diacylglycerides,  
846 and development of a fluorogenic substrate for sulfoquinovosidases. *Org. Biomol. Chem.*  
847 **18**, 675-686 (2020).
- 848 29. A. B. Blakeney, L. L. Mutton A simple colorimetric method for the determination of sugars  
849 in fruit and vegetables. *J. Sci. Food Agric.* **31**, 889-897 (1980).
- 850 30. B. Sörbo (1987) Sulfate: Turbidimetric and nephelometric methods. *Methods Enzymol.*,  
851 (Academic Press), Vol 143, pp 3-6.
- 852 31. G. Brychkova, D. Yarmolinsky, R. Fluhr, M. Sagi The determination of sulfite levels and its  
853 oxidation in plant leaves. *Plant Sci.* **190**, 123-130 (2012).
- 854 32. A. Kurmanbayeva, *et al.* (2017) Determination of Total Sulfur, Sulfate, Sulfite, Thiosulfate,  
855 and Sulfolipids in Plants. *Plant Stress Tolerance: Methods and Protocols*, ed Sunkar R  
856 (Springer New York, New York, NY), pp 253-271.
- 857 33. N. E. Scott, *et al.* Simultaneous glycan-peptide characterization using hydrophilic  
858 interaction chromatography and parallel fragmentation by CID, higher energy collisional  
859 dissociation, and electron transfer dissociation MS applied to the N-linked glycoproteome of  
860 *Campylobacter jejuni*. *Mol. Cell. Proteomics* **10**, M000031-mcp000201 (2011).
- 861 34. J. Rappsilber, M. Mann, Y. Ishihama Protocol for micro-purification, enrichment, pre-  
862 fractionation and storage of peptides for proteomics using StageTips. *Nat. Protoc.* **2**, 1896-  
863 1906 (2007).
- 864 35. J. Cox, M. Mann MaxQuant enables high peptide identification rates, individualized p.p.b.-  
865 range mass accuracies and proteome-wide protein quantification. *Nat. Biotechnol.* **26**, 1367-  
866 1372 (2008).
- 867 36. J. Cox, *et al.* Accurate Proteome-wide Label-free Quantification by Delayed Normalization  
868 and Maximal Peptide Ratio Extraction, Termed MaxLFQ. *Mol. Cell. Proteomics* **13**, 2513  
869 (2014).
- 870 37. S. Tyanova, *et al.* Visualization of LC-MS/MS proteomics data in MaxQuant. *Proteomics*  
871 **15**, 1453-1456 (2015).
- 872 38. Y. Perez-Riverol, *et al.* The PRIDE database and related tools and resources in 2019:  
873 improving support for quantification data. *Nucleic Acids Res.* **47**, D442-d450 (2019).
- 874 39. Mark J. Fogg, Anthony J. Wilkinson Higher-throughput approaches to crystallization and  
875 crystal structure determination. *Biochem. Soc. Trans.* **36**, 771-775 (2008).
- 876 40. M. J. Dagley, M. J. McConville DExSI: a new tool for the rapid quantitation of <sup>13</sup>C-labelled  
877 metabolites detected by GC-MS. *Bioinformatics (Oxford, England)* **34**, 1957-1958 (2018).
- 878 41. W. Kabsch Xds. *Acta Crystallogr., Section D: Biol. Crystallogr.* **66**, 125-132 (2010).

42. P. Evans Scaling and assessment of data quality. *Acta Crystallogr. Sect. D* **62**, 72-82 (2006).
43. G. Winter xia2: an expert system for macromolecular crystallography data reduction. *J. Appl. Crystallogr.* **43**, 186-190 (2010).
44. L. C. Storoni, A. J. McCoy, R. J. Read Likelihood-enhanced fast rotation functions. *Acta Crystallogr. D Biol. Crystallogr.* **60**, 432-438 (2004).
45. S. Shukla, *et al.* Differential Substrate Recognition by Maltose Binding Proteins Influenced by Structure and Dynamics. *Biochemistry* **57**, 5864-5876 (2018).
46. P. Emsley, K. Cowtan Coot: Model-building tools for molecular graphics. *Acta Crystallogr., Sect. D: Biol. Crystallogr.* **60**, 2126-2132 (2004).
47. G. N. Murshudov, A. A. Vagin, E. J. Dodson Refinement of Macromolecular Structures by the Maximum-Likelihood Method. *Acta Crystallogr. Sect. D* **53**, 240-255 (1997).
48. P. D. Adams, *et al.* PHENIX: a comprehensive Python-based system for macromolecular structure solution. *Acta Crystallogr. D Biol. Crystallogr.* **66**, 213-221 (2010).
49. F. Long, *et al.* AceDRG: a stereochemical description generator for ligands. *Acta Crystallogr. Sect. D* **73**, 112-122 (2017).
50. E. Krissinel, K. Henrick Secondary-structure matching (SSM), a new tool for fast protein structure alignment in three dimensions. *Acta Crystallogr. D* **60**, 2256-2268 (2004).
51. L. Holm, P. Rosenström Dali server: conservation mapping in 3D. *Nucleic Acids Res.* **38**, W545-W549 (2010).
52. S. McNicholas, E. Potterton, K. S. Wilson, M. E. M. Noble Presenting your structures: the CCP4mg molecular-graphics software. *Acta Crystallogr. D* **67**, 386-394 (2011).
53. M. H. Medema, E. Takano, R. Breitling Detecting sequence homology at the gene cluster level with MultiGeneBlast. *Mol. Biol. Evol.* **30**, 1218-1223 (2013).
54. C. L. M. Gilchrist, Y. H. Chooi Clinker & clustermap.js: Automatic generation of gene cluster comparison figures. *Bioinformatics (Oxford, England)*, (2021).
55. P. Yilmaz, *et al.* The SILVA and “All-species Living Tree Project (LTP)” taxonomic frameworks. *Nucl. Acids Res.* **42**, D643-D648 (2013).
56. I. Letunic, P. Bork Interactive Tree Of Life (iTOL) v4: recent updates and new developments. *Nucl. Acids Res.* **47**, W256-W259 (2019).
57. E. W. Deutsch, *et al.* The ProteomeXchange consortium in 2017: supporting the cultural change in proteomics public data deposition. *Nucl. Acids Res.* **45**, D1100-D1106 (2016).

## **Acknowledgements**

Dr Monica Doblin is thanked for the provision of *Agrobacterium tumefaciens* strain C58. This work was supported in part by National Health and Medical Research Council of Australia (NHMRC) project grants GNT1100164 (N.E.S), GNT1174405 (D.B.A.), GNT1139546 and GNT1139549 (E.D.G.-B); the Leverhulme Trust grant RPG-2017-190 (G.J.D.); Australian Research Council grant DP180101957 and DP210100233 (S.J.W.), and DP210100362 (N.E.S.); and support from The Walter and Eliza Hall Institute of Medical Research, the Australian Cancer Research Fund and a Victorian State Government Operational Infrastructure support grant (E.D.G.-B). G.J.D is supported by the Royal Society Ken Murray Research Professorship, E.D.G.-B. is supported by the Brian M. Davis Charitable Foundation Centenary Fellowship, M.J.M. is an NHMRC Principal Research Fellow, N.E.S. is supported by and Australian Research Council Future Fellowship (FT200100270), B.M. was supported by Melbourne Research Scholarship, J.M. by a Sir John and Lady Higgins Scholarship, M.P. by an Australian Postgraduate Award. We acknowledge Dr. Johan P. Turkenburg and Sam Hart for assistance with X-ray data collection; the Diamond Light Source for access to beamlines I04, i24 and I04-1 under proposal number mx-18598; and the Australian Synchrotron, part of ANSTO, for access to the MX-2 beamline, which made use of the Australian Cancer Research Foundation (ACRF) detector. We thank the 'Melbourne Mass Spectrometry and Proteomics Facility' of the Bio21 Molecular Science and Biotechnology Institute at The University of Melbourne for the support of mass spectrometry analysis and the 'Bioscience Technology Facility' (University of York) for assistance with SEC-MALS analyses.

## **Additional information**

Supplementary information

Correspondence should be addressed to S.J.W, G.J.D or E.D.G.-B.

937 **Figure 1. *A. tumefaciens* utilizes SQ and its glycosides as a carbon source.** (a) Optical density of  
938 *A. tumefaciens* C58 culture (blue) and [SQ] (red), change in [sulfite] (green) and change in [sulfate]  
939 (yellow), with respect to time. This data is representative of two independent experiments (see **Fig.**  
940 **S1**), error bars denote observational error (derived by propagation of estimated random errors). (b)  
941 Manhattan plot of comparative proteomics data for *A. tumefaciens* C58 grown on SQ vs glucose,  
942 demonstrating that the most heavily upregulated proteins belong to a single gene cluster. (c) A  
943 cartoon of the upregulated cluster with automated annotations for each of the gene products. These  
944 would later be renamed *smoABCDEFGHI*, to reflect the importance of the sulfoquinovose  
945 monooxygenase enzyme activity to this new biochemical pathway. (d) A cartoon illustrating the  
946 hypothetical roles played by the gene products of this pathway to complete the catabolism of  
947 SQGro.

948

949 **Figure 2. Biochemical and structural analyses of the SQGro-binding protein SmoF (Atu3282)**  
950 **and SQase SmoI (Atu3285).** (a) Isothermal titration calorimogram for SmoF titrated against its  
951 cognate ligand 2'*R*-SQGro. The data is representative of two independent experiments (see **Fig.**  
952 **S5**). (b) Ribbon diagrams (with transparent surface) for the open and closed (liganded)  
953 conformations of SmoF. 2'*R*-SQGro is bound tightly in the inter-domain cleft and is inaccessible to  
954 the bulk solvent in the closed conformation. (c) Interactions between protein and ligand within the  
955 SmoF•2'*R*-SQGro complex: SmoF is in grey, 2'*R*-SQGro is in green, and the 2Fo – Fc map at 1.5 $\sigma$   
956 is in blue. (d) A cartoon highlighting key interactions from c. (e) Interactions between protein and  
957 ligand within the complex of SmoI-D455N SQase and 2'*R*-SQGro: SmoI is in gold, 2'*R*-SQGro is  
958 in green, and the 2Fo – Fc map at 1.5 $\sigma$  is in blue. (f) A cartoon highlighting key interactions from e:  
959 red spheres represent ordered water molecules; dotted lines represent proposed hydrogen bonds.

960



961

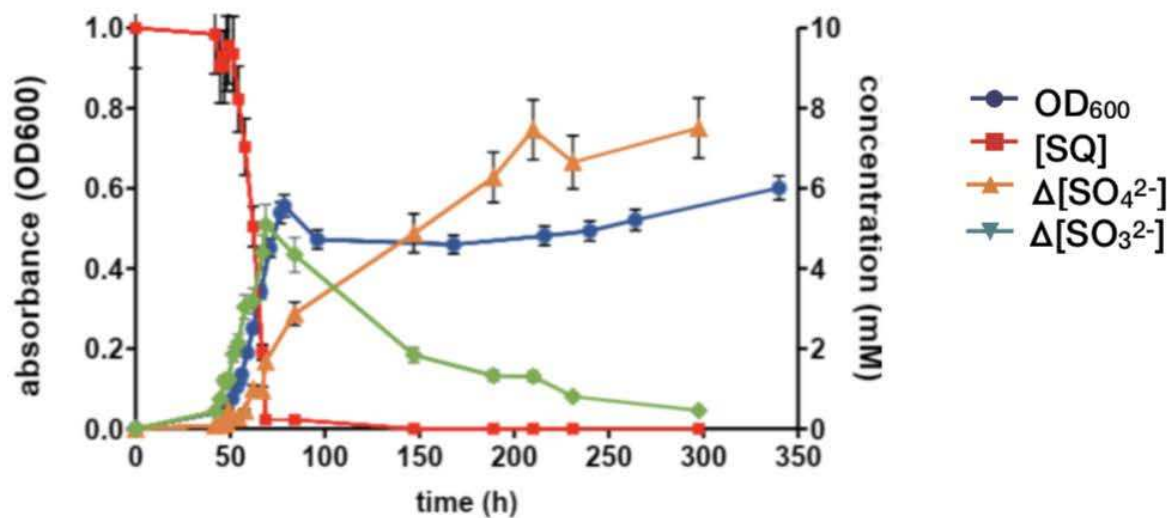
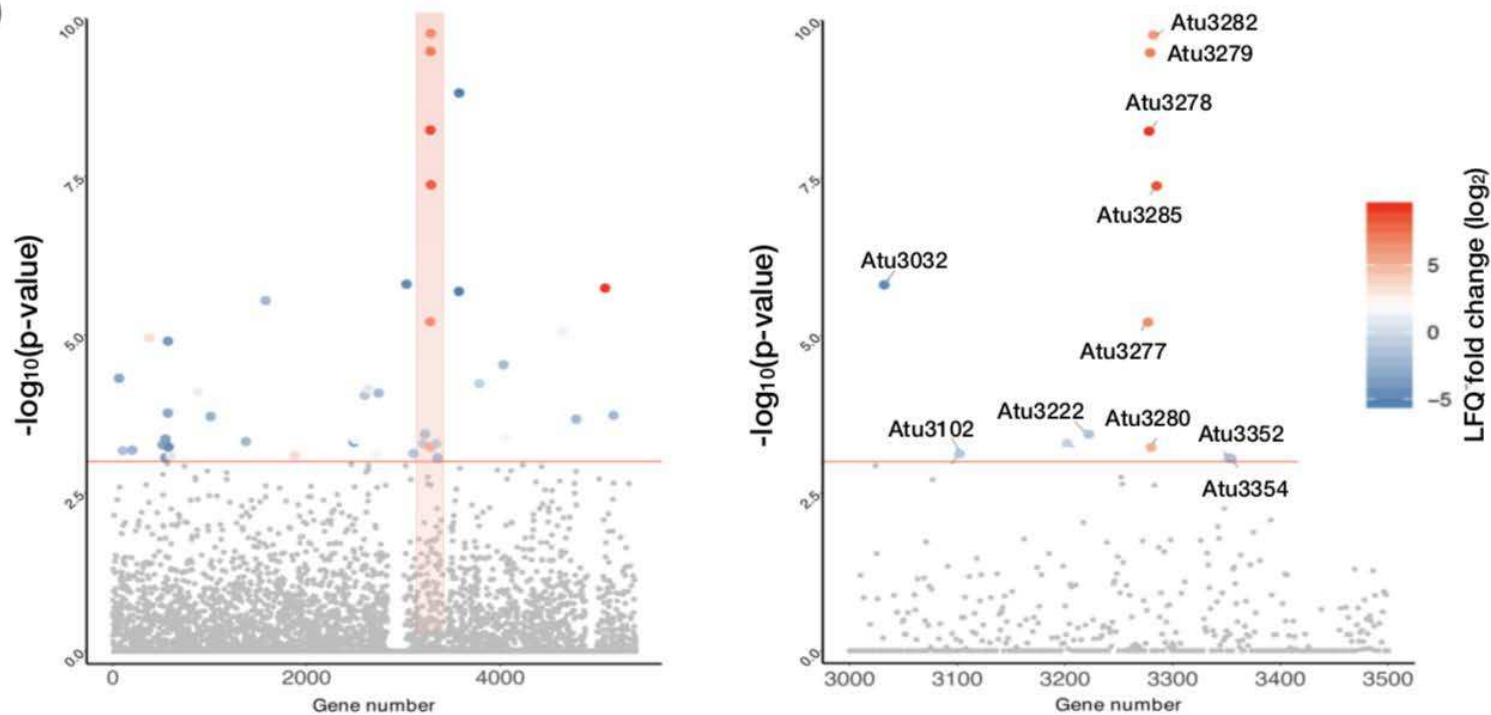
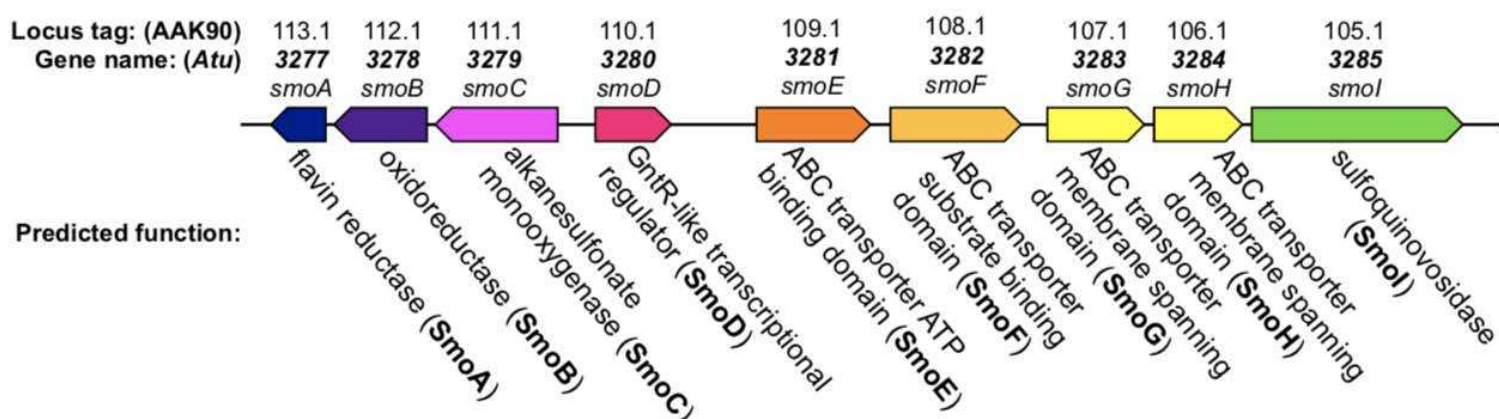
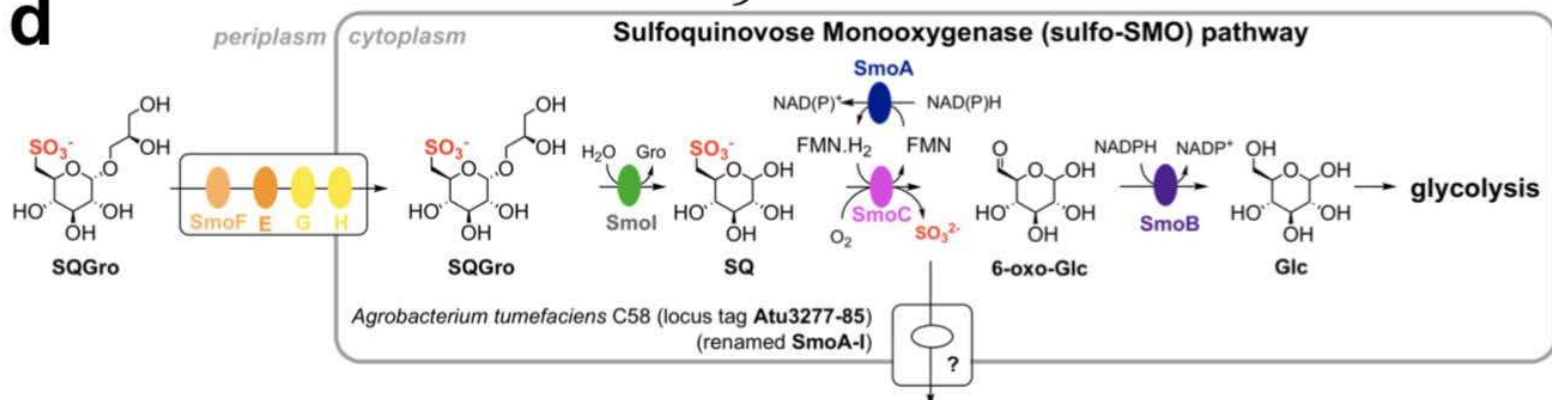
962 **Figure 3. Biochemical and structural analyses of the flavin reductase SmoA and SQ**  
963 **monooxygenase SmoC.** (a) Michaelis-Menten kinetics for SmoA-catalysed reduction of FMN by  
964 NADH. The data is representative of two independent replicates (see **Fig. S10**), error bars denote  
965 observational errors (derived by propagation of estimated random error). (b) SmoC activity assessed  
966 using sulfite release assay with Ellman's reagent in the presence of FMN, flavin reductase, NADH  
967 and SQ. The data is representative of two independent experiments (see **Fig. S11**), error bars denote  
968 observational error (derived by propagation of estimated random errors). (c) Isothermal titration  
969 calorimogram of interaction of SmoC with SQ as determined by ITC. The data is representative of  
970 two independent experiments (see **Fig. S13**). (d) Transparent molecular surface and ribbon diagram  
971 of *RoSmoC* homodimer showing cofactor binding pocket and active site (dotted circle). (e)  
972 Alternative orientation of *RoSmoC* monomer (in gold) overlaid with the MsuD·FMN·CH<sub>3</sub>SO<sub>3</sub><sup>-</sup>  
973 complex (7K14.pdb in ice blue) showing FMN from the latter. Expansion shows view of proposed  
974 substrate-binding pocket and conserved residues lining the active site of *RoSmoC*.

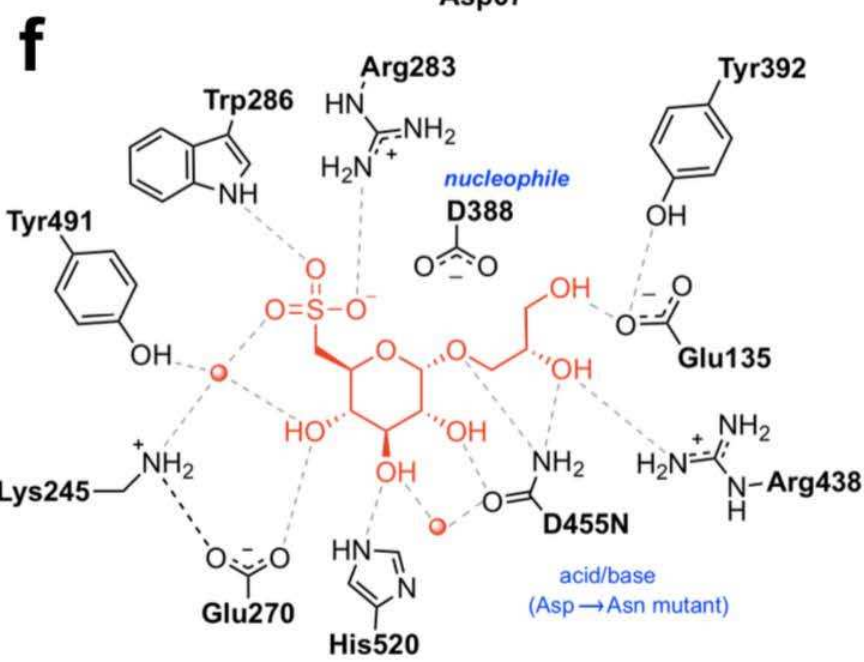
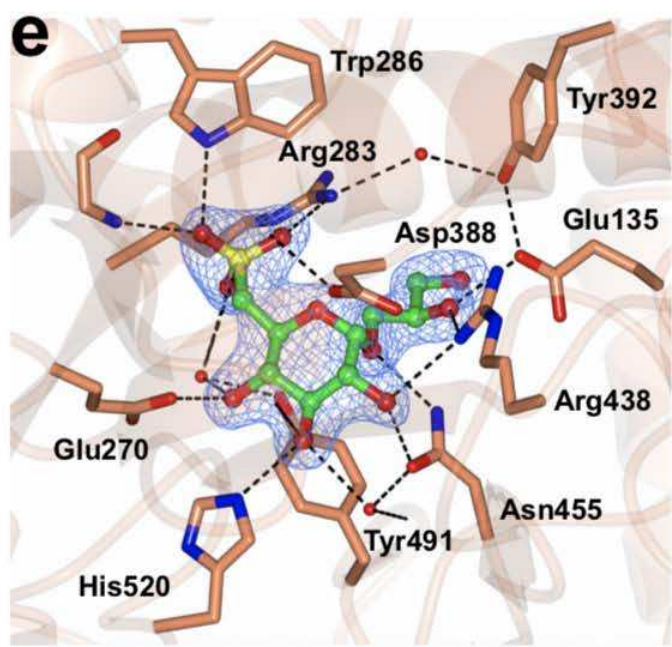
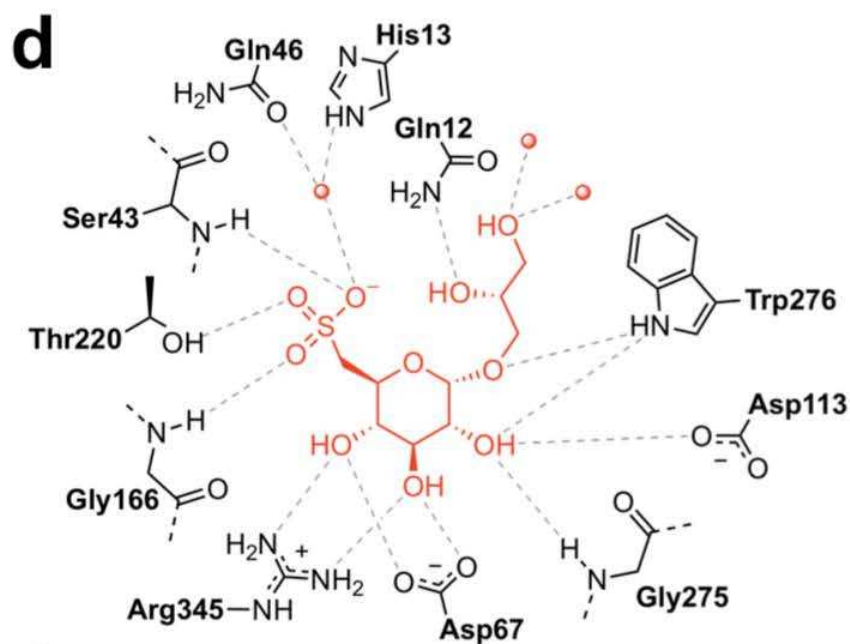
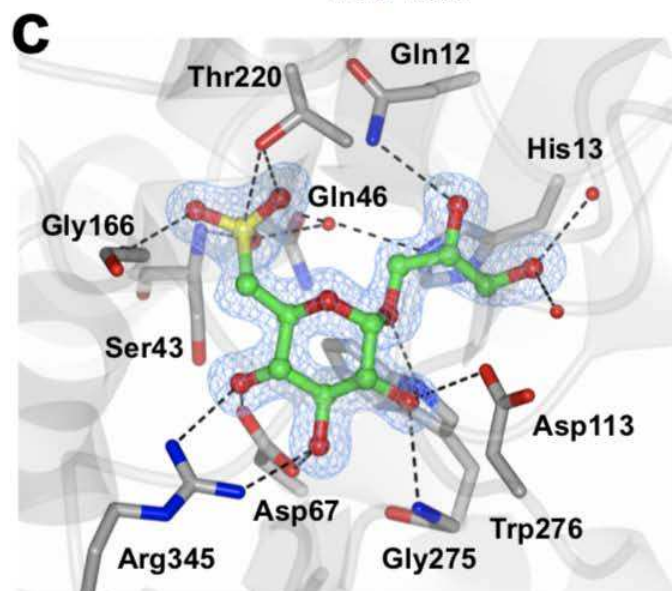
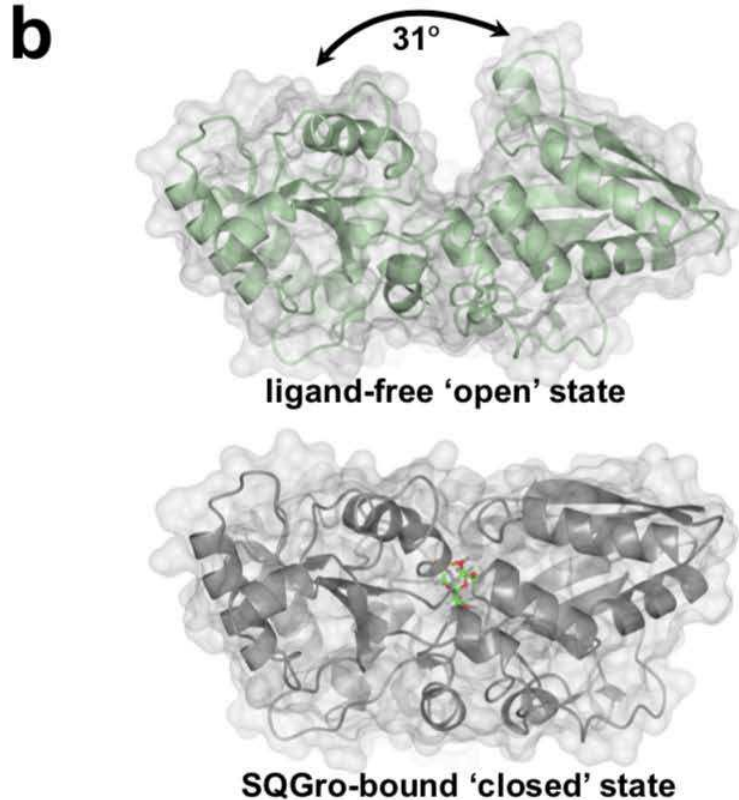
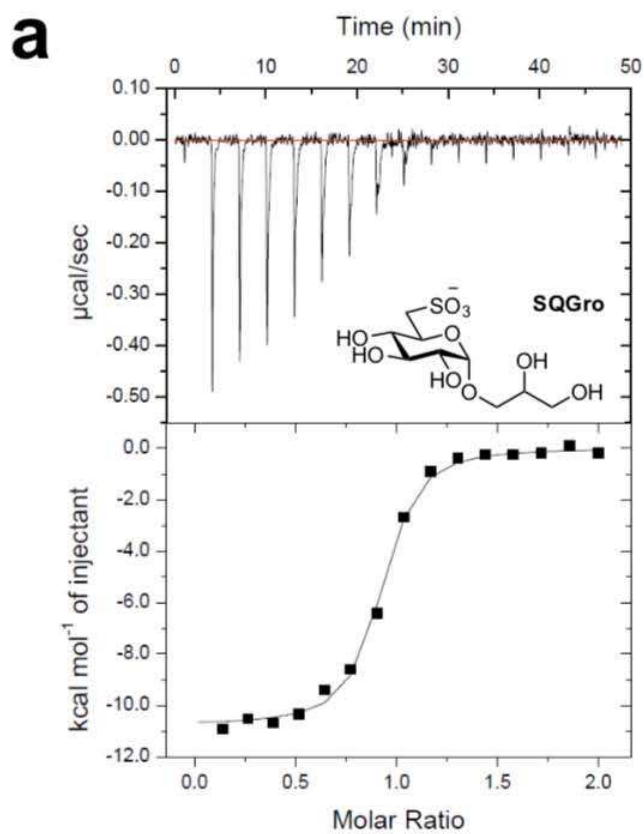
975

976 **Figure 4. Biochemical and structural analyses of 6-oxo-glucose reductase SmoB.** (a) Top:  
977 Equilibrium oxygen exchange at C-6 of Glc via 6-OG facilitated by SmoB when incubated with  
978 NADP<sup>+</sup> in H<sub>2</sub><sup>18</sup>O. Bottom: Derivatization and MS fragmentation allows localization of <sup>18</sup>O to C6 of  
979 Glc. (b) Transparent molecular surface and ribbon diagram of SmoB in complex with NADPH and  
980 Glc. (c) Closeup view of SmoB•NADPH•Glc ternary complex. Backbone and carbon atoms of  
981 SmoB are shown in ice blue and NADPH and glucose are shown in cylinder format. Electron  
982 density for NADPH corresponds to the 2Fo – Fc map in blue at levels of 1σ. (d) Substrate binding  
983 pocket of SmoB depicting hydrogen bonding interactions of glucose with the active site residues  
984 including the conserved catalytic residues Asp71, Lys 104, His151 and Tyr76. Electron density  
985 corresponds to the 2Fo – Fc map (in blue) at levels of 1σ. The geometry of the SmoB-Glc complex  
986 indicates the likely trajectory of hydride addition to 6-OG. (e) Proposed mechanism of SmoB  
987 catalyzed reduction of 6-OG by NADPH showing hydride transfer from C4 of nicotinamide ring of  
988 NADPH to C6 carbonyl and Y76 (within the catalytic tetrad) as the proton donor. The red sphere is  
989 a bound water molecule; dotted lines are proposed hydrogen bonds.

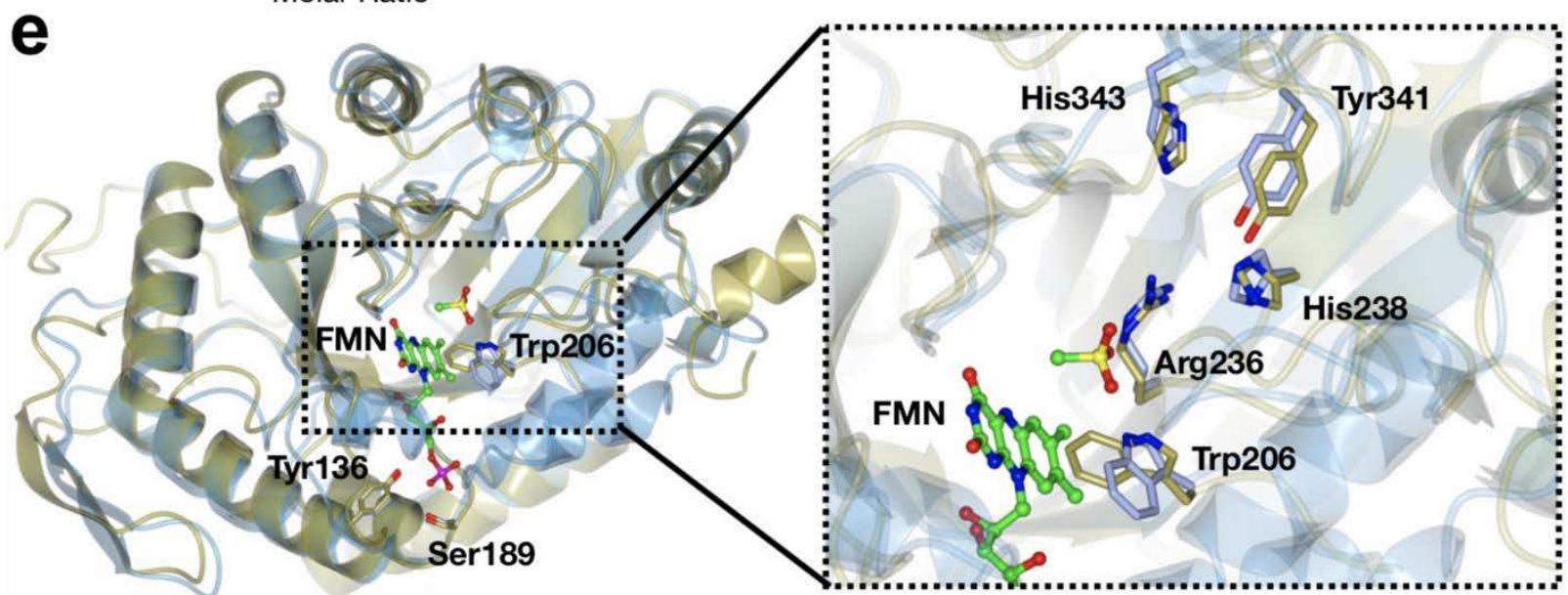
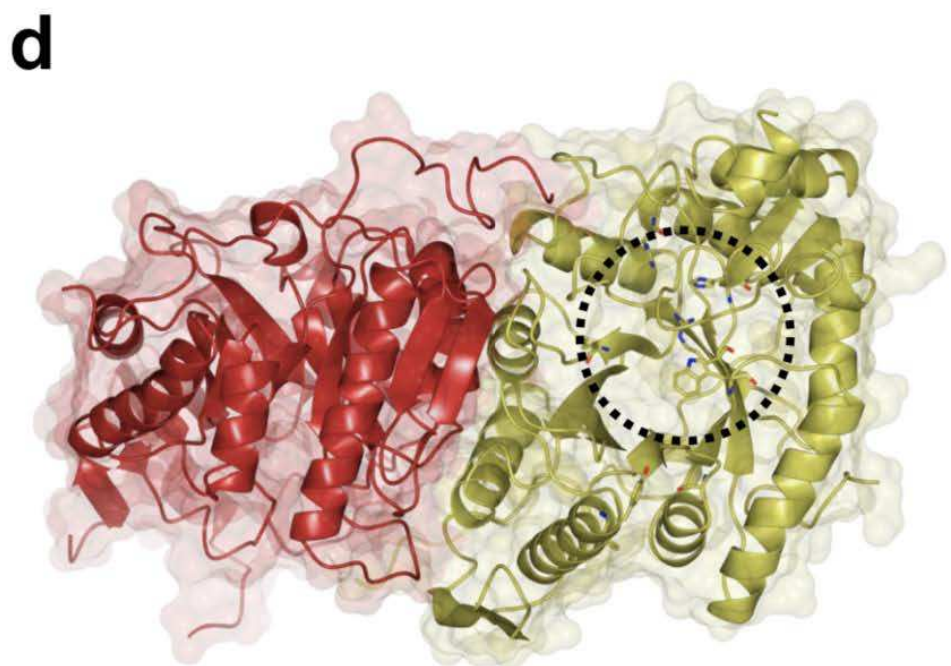
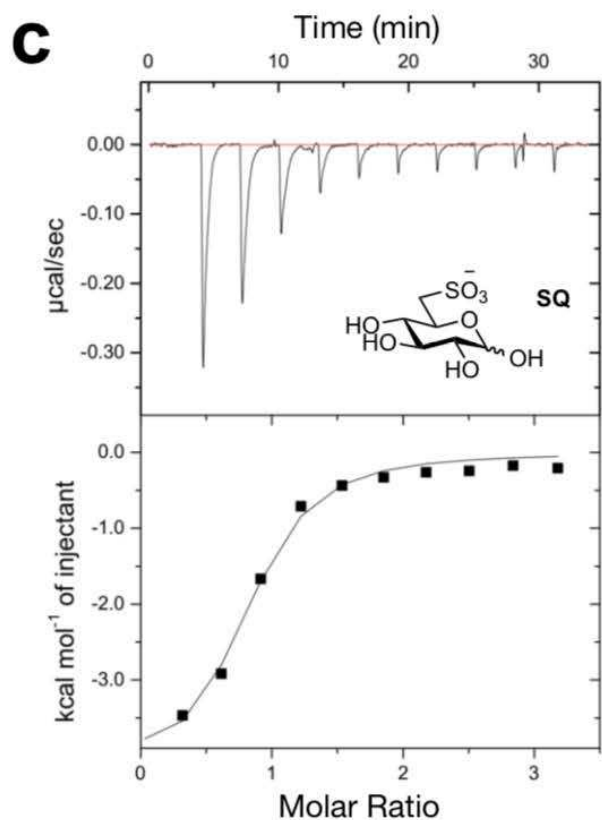
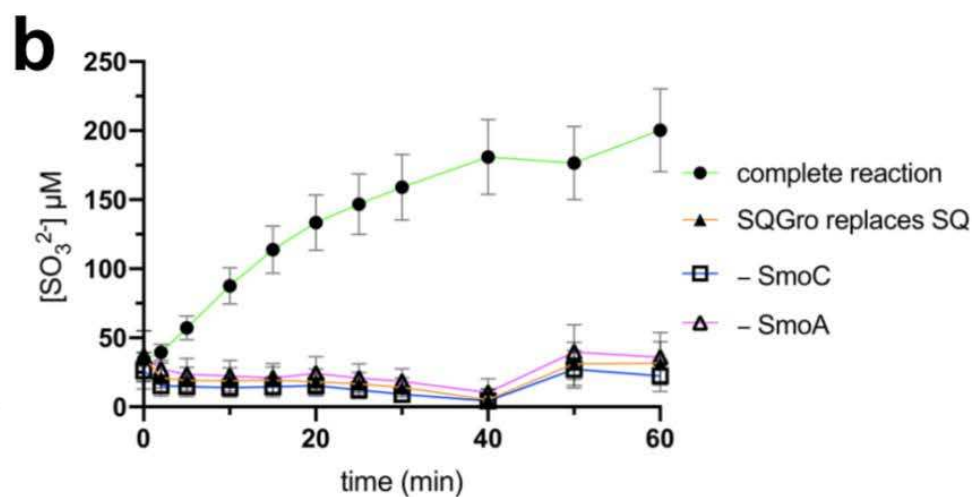
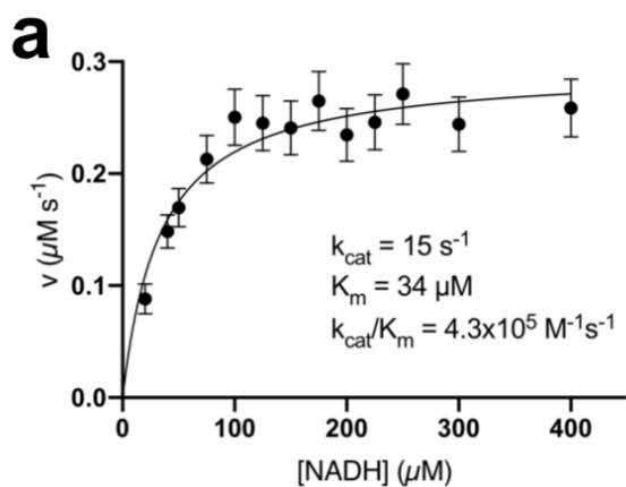
990

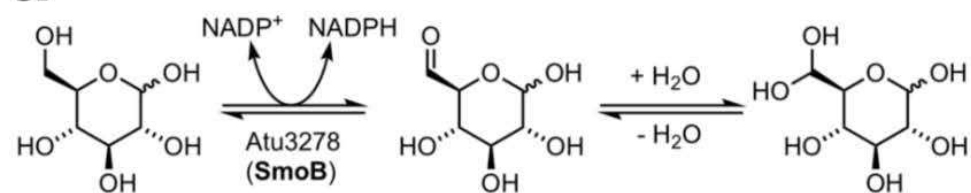
991 **Figure 5. Prevalence of the SMO pathway.** (a) Architecture of the SMO gene cluster in *A.*  
992 *tumefaciens* and homologous gene clusters in other organisms. Colored links indicate  $\geq 30\%$  protein  
993 sequence similarity. Only those clusters encoding putative SQ monooxygenases and SQases were  
994 annotated as putative SMO gene clusters. (b) A phylogenetic tree demonstrating the diversity of  
995 organisms possessing putative SMO gene clusters. The tree was constructed by pruning of the All-  
996 Species Living Tree Project's 16s rRNA-based LTP release 132 ([https://www.arb-](https://www.arb-silva.de/projects/living-tree/)  
997 [silva.de/projects/living-tree/](https://www.arb-silva.de/projects/living-tree/)).

**a****b****c****d**

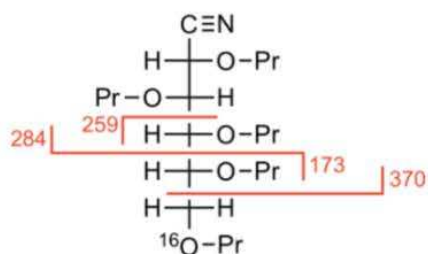
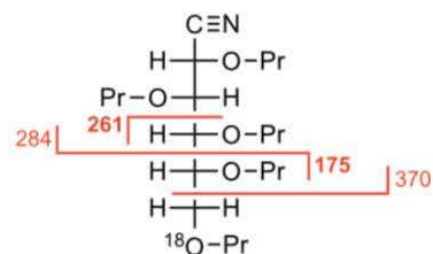
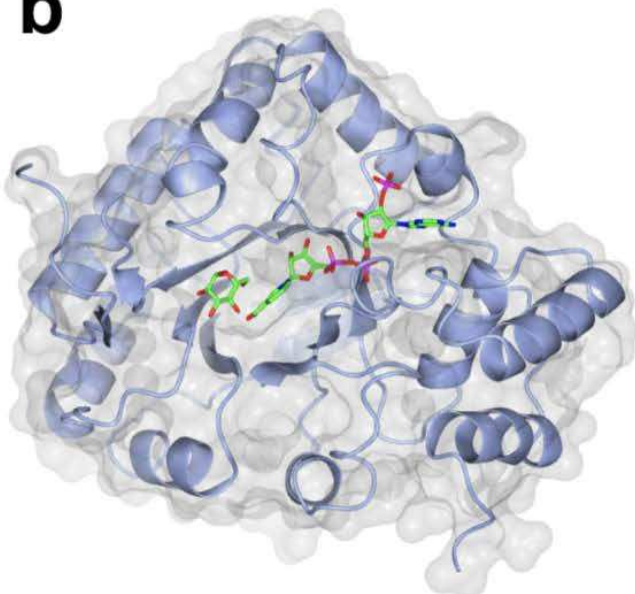
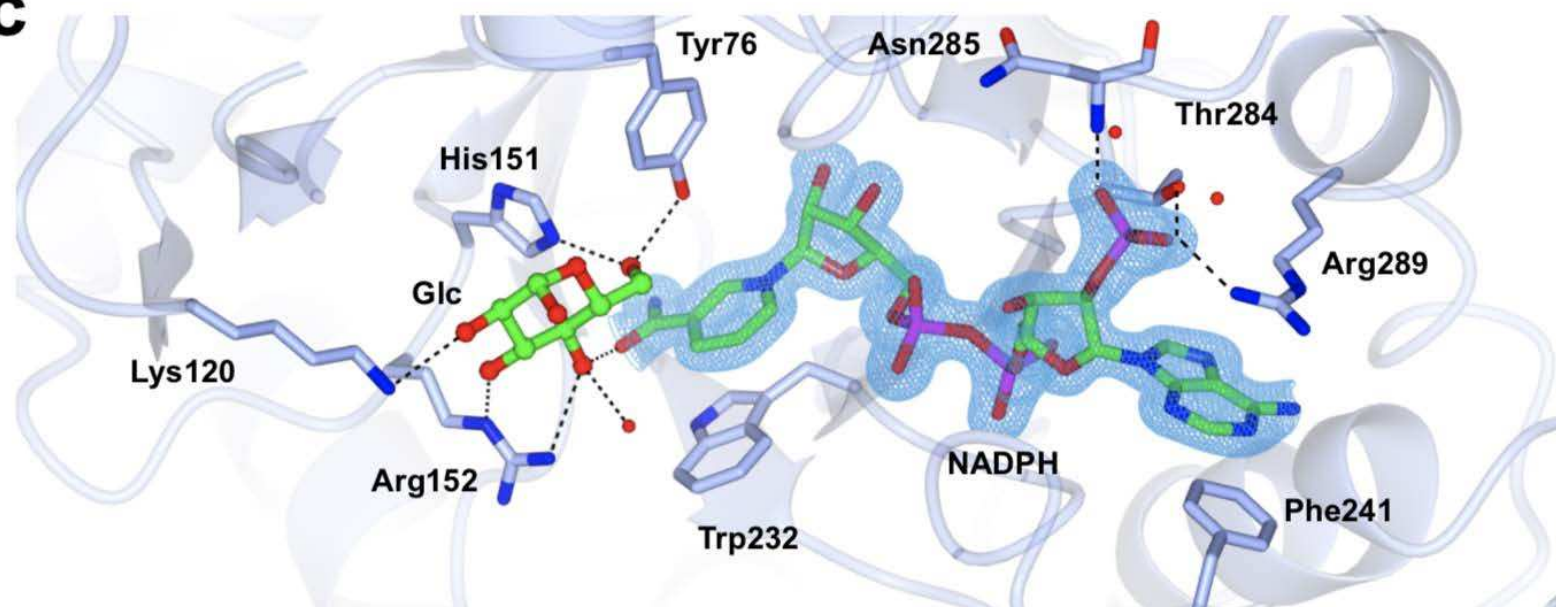
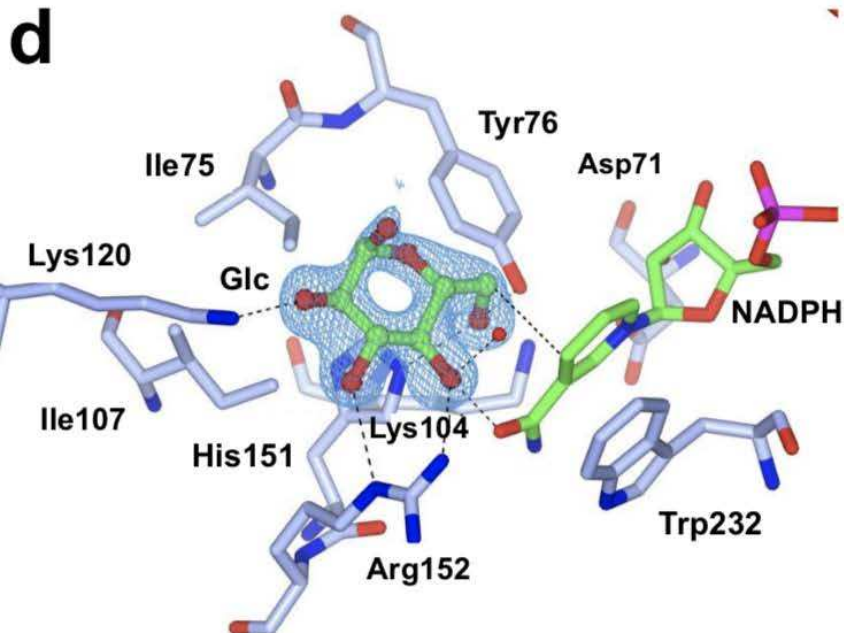
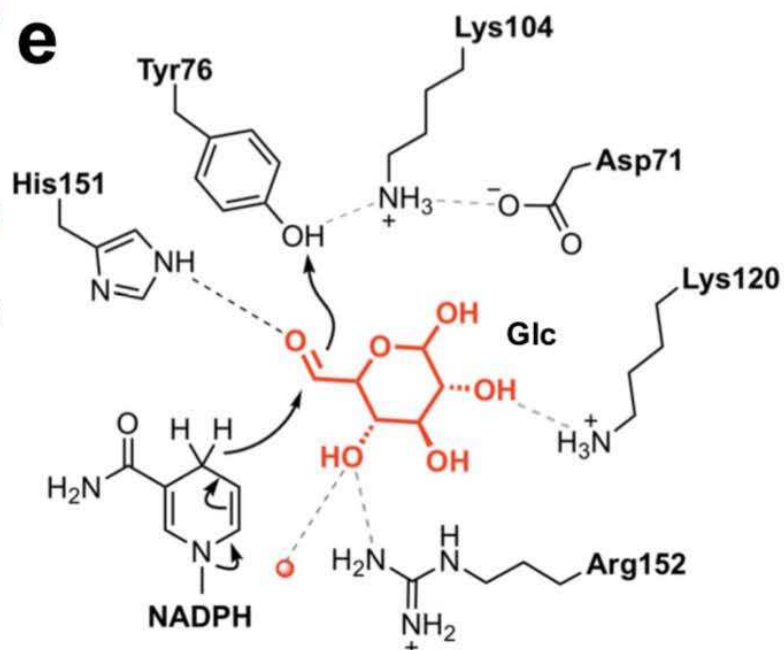




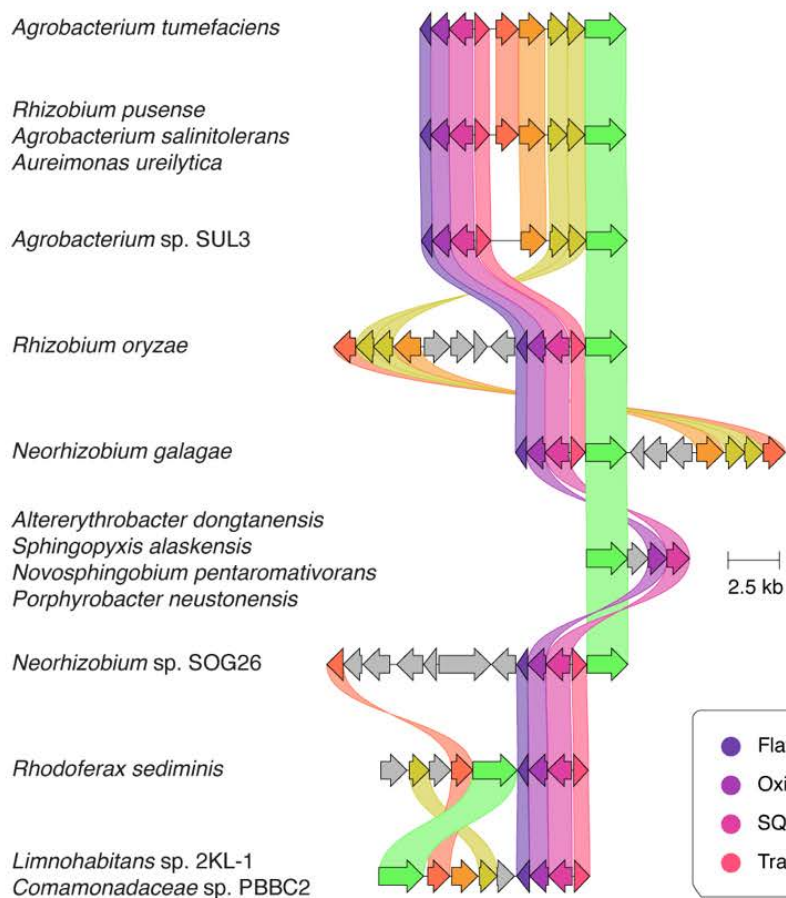


**a**

Unlabelled sample:

 $\text{C6-}^{18}\text{O}$ -labelled:**b****c****d****e**



**a****b**